SOLUTION COMBUSTION SYNTHESIS OF OXIDE SEMICONDUCTORS

by

ABEGAYL LORENDA SHARA-LYNN THOMAS

Presented to the Faculty of the Graduate School of

The University of Texas at Arlington in Partial Fulfillment

of the Requirements

for the Degree of

DOCTOR OF PHILOSOPHY

THE UNIVERSITY OF TEXAS AT ARLINGTON

August 2015

Acknowledgements

The summer of 2015 marks the end of a five year educational accomplishment which started as a dream of a young island girl. The highest respect and esteemed gratitude is given to my research professor, Dr. Krishnan Rajeshwar, for believing in me and allowing me to be part of his research group. His patience, continuous guidance, and unwavering support have made this journey even more meaningful. I extend a special thank you to my committee members, Dr. Peter Kroll and Dr. Kevin Schug, for their encouragement and invaluable advice.

I am extremely grateful to have worked alongside not only local (Dr. Noma de Tacconi, Dr. Muhammed Huda, and Dr. Fuqiang Liu) but international (Dr. Csaba Janaky, Atilla Kormányos) research scholars. I am appreciative of their endless support, research assistance, and just a listening ear. They all made my journey at UTA even smoother. To the past and present members in our group, I say thank you for all your help. Also, thank you to The University of Texas at Arlington and the Sid Richardson Carbon & Energy Co. for the opportunity and financial support to pursue and complete my dissertation study.

To my parents Peter & Vilma Thomas: without you giving me a strong foundation to start, this would not have been possible. Thanks for pushing me and all the tough love getting me to this point of my life. My sisters Shemeika Williams and Andrea Thomas: your emotional support and many breaks to be with you put it all in perspective. To all my other family members (near and far) who asked about my progress and called to check up on me: thank you.

Last but not least, to the best husband in the world, Peter McMillan, and my wonderful son: Jonathan McMillan; it has been quite a journey getting to this point. However, you both are my rock and here with me sharing this moment. So many great

things have happened through these past few years, and Peter: your undying love, encouragement, and moral support made it easier and all worth it.

"The future belongs to those who believe in the beauty of their dreams."

Eleanor Roosevelt.

July 14, 2015

Abstract

SOLUTION COMBUSTION SYNTHESIS OF OXIDE SEMICONDUCTORS

Abegayl Lorenda Shara-Lynn Thomas, PhD

The University of Texas at Arlington, 2015

Supervising Professor: Krishnan Rajeshwar

The quest for stable and efficient photocatalytic materials beyond TiO_2 and WO_3 has over the years led to the development of new materials that possess more optimal interfacial energetics. This dissertation study focused on using for the first time a novel method, solution combustion synthesis (SCS), to prepare two distinct families of binary metal-based oxide semiconductor materials. Detailed studies on material characteristics and applications were carried out on tungsten- and niobium-based oxide semiconductors with varying principal metals.

Initial emphasis was placed on the SCS of tungsten-based oxide semiconductors ($ZnWO_4$, $CuWO_4$, and Ag_2WO_4). The influence of different tungsten precursors on the resultant product was of particular relevance to this study, with the most significant effects highlighted. Upon characterization, each sample's photocatalytic activity towards methyl orange dye degradation was studied, and benchmarked against a commercial oxide sample obtained by solid-state ceramic synthesis.

Detailed analysis highlighted the importance of the SCS process as a time- and energy-efficient method to produce crystalline nano-sized materials even without additional or excessive heat treatment. It was observed that different tungstate precursors do influence the structural and morphological make-up of the resulting

materials. The as-synthesized tungstate materials showed good photocatalytic performance for the degradation of methyl orange dye, while taking into account specific surface area and adsorbed dye amount on the surface of the material.

Like the tungstates, niobium-based oxide semiconductors $CuNb_2O_6$ and $ZnNb_2O_6$ were synthesized for the first time via SCS. Particular attention was placed on the crystal structures formed while using an oxalate niobium precursor during the reaction process. X-ray diffraction patterns yielded a multiphase structure for the $ZnNb_2O_6$ and a single phase structure for $CuNb_2O_6$. Photoelectrochemical (PEC) measurements were used both as a characterization tool as well as an application for CO_2 reduction. The PEC data were consistent with an n-type and p-type semiconductor for $ZnNb_2O_6$ and $CuNb_2O_6$ respectively. Good phototelectrochemical behavior was observed for $CuNb_2O_6$ with stable, high photocurrents suggesting a suitable material for CO_2 reduction in 0.1 M $NaHCO_3$ + CO_2 medium.

Overall, this study illustrates the utility of SCS for the time- and energy-efficient synthesis of metal tungstates and niobates for solar energy conversion and environmental remediation applications.

Table of Contents

Acknowledgements iii

Abstract v

List of Illustrations ix

List of Tables xiii

Chapter 1 Oxide Semiconductors for Environmental Remediation 1

1.1. Overview of Semiconductor Prototypes 1

1.1.1. General Principles of Semiconductor Materials 4

1.1.2. Photocatalysis 6

1.2. Preparative Methods for Oxide Semiconductors 10

1.2.1. Solution Combustion Synthesis 11

Chapter 2 Band Engineering and Underlying Solid State Chemistry 14

2.1. Tungsten-based Oxide Semiconductors 14

2.2. Niobium-based Oxide Semiconductors 19

Chapter 3 Preparative Methods and Materials Characterization 23

3.1. Tungsten-based Oxide Semiconductors 23

3.1.1. Materials 23

3.1.2. Solution Combustion Synthesis 23

3.2. Niobium-based oxide semiconductors 24

3.2.1. Materials 24

3.2.2. Solution Combustion Synthesis 25

3.3. Physical Characterization Techniques 26

3.3.1. Thermogravimetric Analysis (TGA) 26

3.3.2. Differential Scanning Calorimetry (DSC) 26

3.3.3. X-ray Diffraction (XRD) 27

3.3.4. Diffuse Reflectance Spectroscopy 28
3.3.5. Raman Spectroscopy 29
3.3.6. Electron Microscopy (SEM and TEM) 29
3.3.7. Computational Details 30
3.4. Semiconductor Application Processes 31
3.4.1. Photocatalytic Analysis 31
3.4.2. Liquid Chromatography – Mass Spectrometry (LC-MS) 33
3.5. Photoelectrochemistry 34
Chapter 4 Results and Discussion 35
4.1. Tungsten-based Oxide Semiconductors 35
4.1.1. Thermogravimetric analysis 35
4.1.2. Crystal Structure and Morphology 37
4.1.3. Optical Properties and Electronic Band Structure 52
4.1.4. Photocatalytic Behavior 57
4.1.5. Photoelectrochemical Behavior 65
4.2. Niobium-based Oxide Semiconductors 66
4.2.1. Thermal Analysis 66
4.2.2. Structural and Morphological Determination 67
4.2.3. Optical Properties 72
4.2.4. Electronic Band Structure Calculations 75
Chapter 5 Conclusions 79
References 81
Biographical Information 91

List of Illustrations

Figure 1-1 Electronic energy band representation for solid materials. 5

Figure 1-2 Schematic illustration of the photocatalysis processes that can occur at the surface of a semiconductor particle. 7

Figure 1-3 Factors that may affect the photocatalytic activity of any given semiconductor material. 9

Figure 2-1 Ball and stick representation of the monoclinic WO_3 structure: tungsten – yellow balls and oxygen – red balls. 15

Figure 2-2 Ball and stick model of the crystal structure of $ZnWO_4$. 16

Figure 2-3 Ball and stick model of the crystal structure of $CuWO_4$. 17

Figure 2-4 Ball and stick model of the crystal structure of Ag_2WO_4. 17

Figure 2-5 Schematic representation of approximate conduction and valence band edge positions of the binary tungsten-based oxides. The interfacial energetics for TiO_2 and WO_3 are also shown for comparison. 19

Figure 2-6 Polyhedral model of the crystal structure for $ZnNb_2O_6$. 21

Figure 2-7 Polyhedral model of the crystal structure for $CuNb_2O_6$. 22

Figure 3-1 Flowchart of the solution combustion synthesis reaction procedure. 25

Figure 3-2 Diagram of the photocatalytic reactor utilized with powder semiconductor materials. 32

Figure 4-1 TGA profiles of the SCS precursor mixtures for $CuWO_4$. 36

Figure 4-2 DSC profiles of the SCS precursor mixtures for $CuWO_4$ 37

Figure 4-3 XRD patterns for $ZnWO_4$ samples. (*) represents the presence of the WO_{3-x} in the synthesized samples. 38

Figure 4-4 XRD patterns for $CuWO_4$ samples. (*) represents the presence of the WO_{3-x} in the synthesized samples. 39

Figure 4-5 XRD patterns for Ag_2WO_4 samples. (*) represents the presence of the WO_{3-x} in the synthesized samples. 40
Figure 4-6 Rietveld refinement of A – B $ZnWO_4$ (Na) and $ZnWO_4$ (NH_4) respectively; C – D $CuWO_4$ (Na) and $CuWO_4$ (NH_4) respectively; and E – F Ag_2WO_4 (Na) and Ag_2WO_4 (NH_4) respectively. 44
Figure 4-7 TEM images of A-B $CuWO_4$ (Na) as-synthesized and annealed at 400°C respectively; C-D $ZnWO_4$ (Na) as-synthesized and annealed at 500°C respectively; E-F $ZnWO_4$ (NH_4) as-synthesized and annealed at 500°C respectively; G-H Ag_2WO_4 (NH_4) as-synthesized and annealed at 500°C. 47
Figure 4-8 I and J are HR-TEM images of the nanoparticles in Figure 4-7 A and E. 48
Figure 4-9 Raman spectra of $ZnWO_4$ (Na), $CuWO_4$ (Na), and Ag_2WO_4 (Na) samples. 48
Figure 4-10 Tauc plots showing band gap values for $ZnWO_4$ samples. 52
Figure 4-11 Tauc plots showing band gap values for $CuWO_4$ samples. 53
Figure 4-12 Tauc plots showing band gap values for Ag_2WO_4 samples. 53
Figure 4-13 Photographs of the SCS tungstate samples using Na_2WO_4. 54
Figure 4-14 Electronic band structure for $ZnWO_4$. 56
Figure 4-15 Electronic band structure for $CuWO_4$. 56
Figure 4-16 Electronic band structure for Ag_2WO_4. 57
Figure 4-17 Methyl orange photodegradation using the as-synthesized $ZnWO_4$ samples under UV – Visible light irradiation. 58
Figure 4-18 Methyl orange photodegradation using the as-synthesized $CuWO_4$ samples under UV – Visible light irradiation. 59
Figure 4-19 Methyl orange photodegradation using the as-synthesized Ag_2WO_4 samples under UV – Visible light irradiation. 59

Figure 4-20 LC-MS monitoring of methyl orange degradation using $ZnWO_4$ (Na) under UV-visible light irradiation.....60
Figure 4-21 Comparison of the linear regression apparent rate constant values from methyl orange photodegradation. 62
Figure 4-22 Adsorption kinetics of methyl orange on $ZnWO_4$ (NH_4, as-is) with a 2 g/L catalyst concentration and 50 µM methyl orange solution concentration. 64
Figure 4-23 Comparison of the specific-, and surface area normalized amounts of adsorbed methyl orange for the different tungstate samples. The catalyst concentration was 2 g/L, while the concentration of the methyl orange solution was 200 µM. 64
Figure 4-24 A. Photovoltammogram of a $CuWO_4$ (NH_4) sample recorded between 0.1 V and 1.1 V, in 0.1 M Na_2SO_4, at a sweep rate of 2 mV s^{-1} using a 300W Hg-Xe arc lamp. B. Comparison of the onset potential for the three tungstate samples in 0.1 M Na_2SO_3. 66
Figure 4-25 A. TGA and B. DSC profiles of the copper and zinc niobate precursor mixtures.....68
Figure 4-26 XRD patterns of A. $ZnNb_2O_6$ and B. $CuNb_2O_6$ samples; (*) represents the presence of ZnO in the sample and Nb_2O_5 in $ZnNb_2O_6$ and $CuNb_2O_6$ respectively.....69
Figure 4-27 SEM images of A-B. $ZnNb_2O_6$ as-synthesized and annealed at 600°C respectively and C-D. $CuNb_2O_6$ as-synthesized and annealed at 600°C respectively.....71
Figure 4-28 TEM images of A-B $ZnNb_2O_6$ and $CuNb_2O_6$ annealed at 600°C respectively and C-D HR-TEM images of images A, B respectively, displaying the presence of lattice fringes.....72
Figure 4-29 Photographs of A. $ZnNb_2O_6$ and B. $CuNb_2O_6$. 73
Figure 4-30 Tauc plot of $ZnNb_2O_6$ annealed at 600˚C. The insert shows the band gap determination for ZnO. 74
Figure 4-31 Tauc plot of $CuNb_2O_6$ annealed at 600˚C. 75

Figure 4-32 Electronic band structure of A. $ZnNb_2O_6$ and B. $CuNb_2O_6$. 76

Figure 4-33 Photovoltammogram of $ZnNb_2O_6$ in 0.1 M Na_2SO_3 at a sweep rate of 2 mV/s using a 100 W Oriel UV lamp. 77

Figure 4-34 Photovoltammogram of $CuNb_2O_6$ at sweep rate of 1 mV/s using a Fiberlite visible lamp. 78

List of Tables

Table 1-1 Commonly studied semiconductor materials other than TiO_2 and WO_3. 3

Table 3-1 Synthesized samples prepared from different tungsten precursors. 24

Table 4-1 Calculated average crystallite sizes of the various tungstate samples as a function of annealing and tungstate precursor. 43

Table 4-2 Raman vibrations of SCS $ZnWO_4$ 49

Table 4-3 Raman vibrations of SCS $CuWO_4$. 50

Table 4-4 Raman vibrations of SCS Ag_2WO_4. 51

Table 4-5 Optical properties of the synthesized samples using different tungsten precursors. 53

Table 4-6 Apparent rate constants for MO photodegradation. 61

Table 4-7 BET surface area values for the SCS tungstate samples and commercial benchmarks 63

Table 4-8 Calculated average crystallite sizes and surface area values for the SCS niobate samples as a function of annealing temperature. 70

Table 4-9 Optical properties of the solution combustion synthesized niobate samples. .. 73

Chapter 1

Oxide Semiconductors for Environmental Remediation

1.1. Overview of Semiconductor Prototypes

The global need to focus on renewable and earth-abundant resources has re-sparked much attention on inorganic oxide semiconductor materials; many of which are considered attractive candidates for solar energy conversion[1,2,3] and photocatalytic environmental remediation.[4,5] They are attractive candidates for such applications since they possess an array of desirable characteristics:

- good optical properties (absorption within the visible light spectrum)
- chemically inertness
- photo- and chemical stability in aqueous solutions of varying pH
- good photoelectrochemical and/or photocatalytic behavior
- suitable band edge positions ideal for the generation of oxidizing and reducing species at the semiconductor/medium interface
- efficient excited electron – hole (e^- - h^+) generation, separation, and migration to the semiconductor surface

To date, titanium dioxide (TiO_2) has been the most extensively studied oxide, due to its excellent photoelectrochemical and photocatalytic behavior.[6] It is quite a versatile material in that it has been used in various applications, including and not limited to water splitting for hydrogen evolution,[4,7] water purification (removal of toxic organic pollutants and reduction of dissolved metal ions),[8-10] and inactivation of microbial populations.[11,12] However, TiO_2 has a relatively wide band gap (~3.0–3.2 eV), thus restricting light absorption to the UV region of the solar spectrum that comprises only ~4% of the solar spectrum. On the other hand, this material exhibits little or no absorption in the visible region (comprising ~50% of the solar spectrum).

Aside from TiO_2, tungsten trioxide (WO_3) has been widely studied; serving as an attractive candidate for both water oxidation and environmental remediation.[13] It shares similar characteristics to TiO_2 in terms of chemical inertness, and photo- and chemical stability in aqueous solutions in a relatively broad pH range. Importantly, WO_3 has a band gap energy (E_g) of 2.7 eV (vs. 3.2 eV TiO_2), with its absorption edge located just at the cusp of the visible light spectrum. However, it lacks the ability for spontaneous hydrogen evolution by photogenerated electrons because it has a more positive flat-band potential.[14]

Although TiO_2 and WO_3 have been two of the most widely studied oxide semiconductors, there are other binary oxide semiconductors (e.g., ZnO, Fe_2O_3) that have been considered within this scope of research. They however, possess many more drawbacks than the aforementioned materials limiting their application abilities. Table 1-1 below highlights some of the application possibilities considered for some popular oxide semiconductors other than TiO_2 and WO_3.

Based on these considerations and recognition of the critical need to develop new materials families, one of the challenges put forward is developing materials with altered energy band gaps that can harness the more abundant visible light in the solar spectrum. Henceforth, the quest for other materials besides the TiO_2 and WO_3 prototypes has vastly increased over the last two decades. As a result, appreciable efforts have been devoted to the shifting of band edge positions of various semiconductor materials ("bandgap engineering") to tailor the interfacial energetics of the materials for specific applications by doping or alloying.[1,14] More in-depth discussions into the semiconductor materials bandgap engineering will be discussed later. However, before moving forward, a brief review below gives some basic knowledge about semiconductors pertaining to

bands and their positioning, bandgap energy, and the role these materials play in photocatalytic reactions.

Table 1-1 Commonly studied semiconductor materials other than TiO_2 and WO_3.

Oxide	E_g (eV)	Highlighted Studies/Limitations	References
ZnO	3.2	Direct band gap with good thermal conductivity. Photocorrosion of the material occurs under UV irradiation; ZnO also suffers from dissolution at extreme pH.	15 – 18
Fe_2O_3	2.2	Varied thin films and nanostructured forms applied for organic pollutant degradation and PEC water splitting. Main drawback is facile electron/hole recombination.	19 – 22
Bi_2O_3	2.8	Low stability. Reports show that different synthesis methods do help in improving the material's performance.	23 – 25

Table 1-1 - Continued

Cu_2O	2.1 – 2.5	Studies tend to focus on solar energy conversion with limited and conflicting reports on water photoelectrochemistry. The material does experience anodic and cathodic photocorrosion, along with oxidative decomposition in air.	26 – 28
SnO_2	3.5 – 3.7	High band gap and stable material. Comparable properties to TiO_2; however, usually a component of a semiconductor composite material due to its unsatisfactory photocatalytic activity when used alone.	29 – 31

1.1.1. General Principles of Semiconductor Materials[32]

A semiconductor is generally described as a material that has intermediate electrical conductivity at room temperature, and increases with the input of energy. However, the overall electrical behavior of semiconductors is described via the band model, involving electrons moving from different energy levels forming *bands*. Within a given semiconductor material, there consists of a fully electron occupied *valence band* (VB) and an unoccupied *conduction band* (CB). The separation (gap) between the valence and the conduction band is known as the *energy band gap* (E_g) normally expressed in electron volts (eV), see Figure 1-1. For semiconductor materials, poor conductivity exists at room temperature, and increases with the input of thermal or light energy. Compared to their metal (very small band gap) or insulator (very large band gap)

counterparts, semiconductors usually have a moderately spaced band gap, resulting in electrons moving freely from the valence band to the conduction band causing conduction to be possible.

A small band gap is considered a good semiconductor material because only a small amount of energy will be required to facilitate charge transfer. On the other hand, a larger semiconductor band gap can increase the possibility of charge recombination and transfer to the semiconductor interface. For this reason, thermal excitation is necessary to increase the electrical mobility of the material.

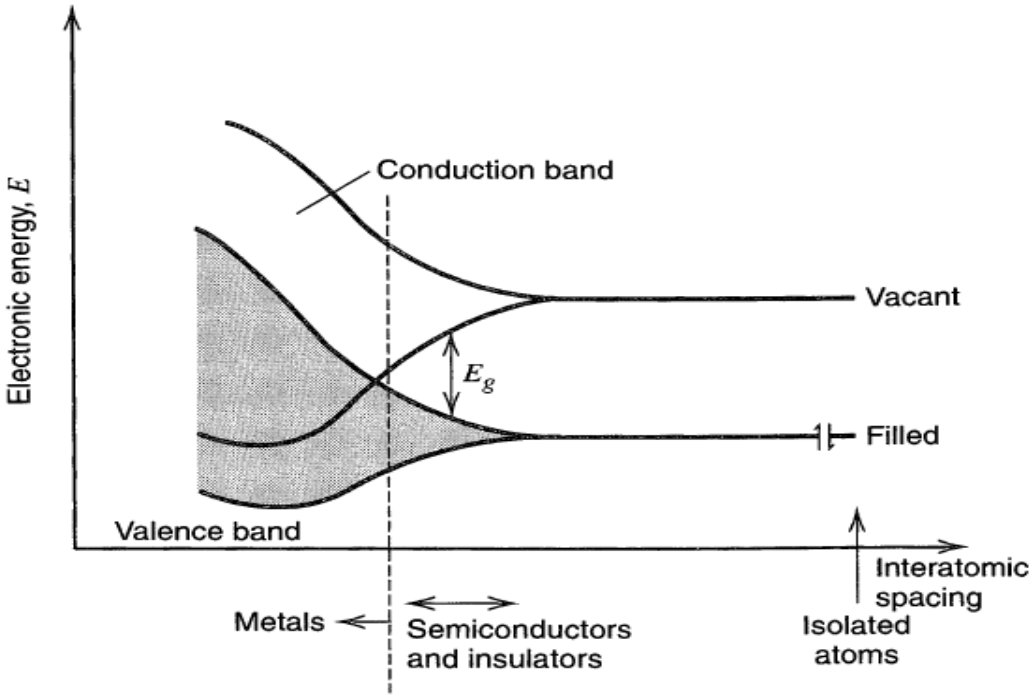

Figure 1-1 Electronic energy band representation for solid materials.

As duly noted, the size of the band gap is highly influential in the optical and photocatalytic properties of a semiconductor material as will be seen throughout this study. A material that possesses band edges positioned above the threshold necessary for hydrogen reduction and water oxidation is quite suitable to be used to allow various redox reactions to occur on its surface. With that in mind, the most suitable material would also absorb light within the solar spectrum, thus having an $E_g < 3.0$ eV.

1.1.2. Photocatalysis

Photocatalysis is an expanding science that utilizes solids notably semiconductors to promote reactions via charge carriers in the presence of light which in turn increases the electrical conductivity of a semiconductor material. When a semiconductor material is irradiated with light, one of two things can happen as the photons hit the semiconductor surface. If the photon energy ($h\nu$) is lower than the band gap energy of the semiconductor, it will pass through the semiconductor. But, if the photon energy is greater than the band gap energy of the semiconductor, this energy is absorbed by the material.

The absorbed photon energy causes an electron (e_{CB}^-) to be promoted from the valence band to the conduction band, thus leaving behind a positively charged hole (h_{VB}^+) which also can "move" around the valence band. The generated electron – hole (e^- - h^+) pair (charge carrier, exciton) migrates to the surface of the semiconductor causing redox reactions to occur. Electrons found in the conduction band can reduce H_2O to H_2, while the holes in the valence band can oxidize H_2O yielding O_2 (water splitting).[33] As for organic pollutants, oxidation reactions occur as photogenerated $OH^\bullet$ (hydroxyl radicals) and superoxide ions ($O_2^{\bullet-}$) attack different carbon atoms within the pollutant.[34] The oxidation reactions mineralize the parent organic pollutant to simpler molecules to

(ultimately) complete mineralization to CO_2 and H_2O.[35,36] Figure 1-2 shows a schematic illustration of the photocatalysis processes that can occur in a semiconductor particle.

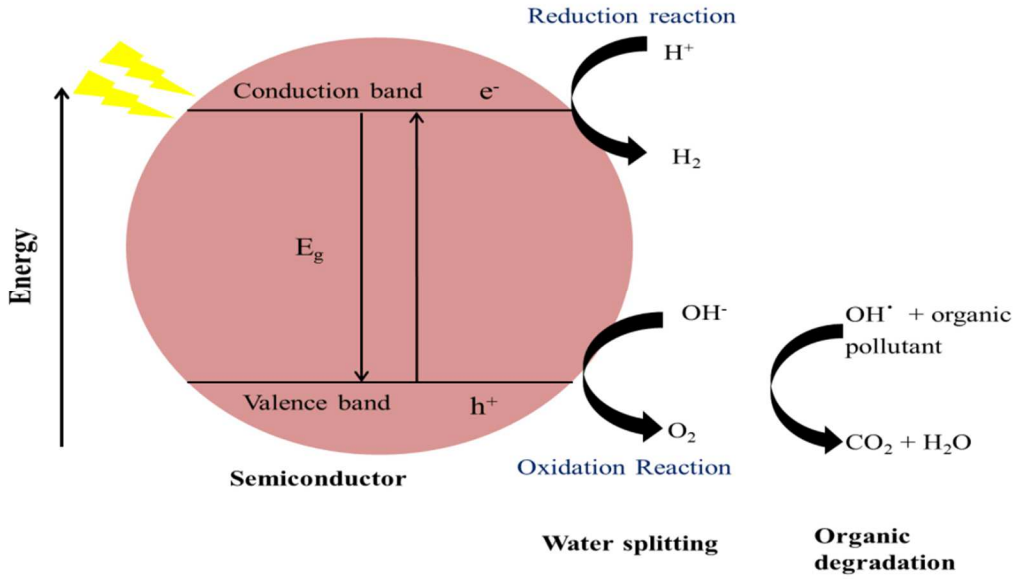

Figure 1-2 Schematic illustration of the photocatalysis processes that can occur at the surface of a semiconductor particle.

Recombination is also possible during a photocatalytic reaction if there is limited oxygen available. The presence of oxygen serves to scavenge the photogenerated electrons, thus forming superoxides. All in all, only the molecules in direct contact with the semiconductor material surface can undergo photocatalysis. To date, many reaction

mechanisms have been postulated where initial photo-excitation of the semiconductor particle activates the entire photocatalysis process.

The basic steps for any given semiconductor material are as follows:[37-39]

Photo-excitation: $SC + hv \rightarrow SC\ h_{VB}^{+} + SC\ e_{CB}^{-}$ (1)

Charge carrier trapping: $SC - OH + h_{VB}^{+} \rightarrow [SC - OH^{\bullet}]^{+}$ (2)

$SC - OH + e_{CB}^{-} \rightarrow [SC - OH^{-}]$ (3)

Charge carriers can recombine in various ways, mostly non-radiative.

Bulk recombination: $SC\ h_{VB}^{+} + SC\ e_{CB}^{-} \rightarrow SC + heat$ (4)

Charge-carrier recombination:

$h_{VB}^{+} + [SC - OH^{-}] \rightarrow SC - OH$ (5)

$e_{CB}^{-} + [SC - OH^{\bullet}]^{+} \rightarrow SC - OH$ (6)

Organic mineralization process:

$SC\ h_{VB}^{+} + H_2O \rightarrow SC - OH^{\bullet} + H^{+}$ (7)

$M + OH^{\bullet} \rightarrow$ dye intermediates $\rightarrow CO_2 + H_2O$ (8)

$O_2 + e_{CB}^{-} \rightarrow O_2^{\bullet -}$ (9)

$M + e_{CB}^{-} \rightarrow M_{red}$ (10)

where SC – semiconductor; h_{VB}^{+} – valence band hole; e_{CB}^{-} – conduction band electron; $[SC - OH^{\bullet}]^{+}$ – surface trapped hole (surface bound hydroxyl radical); $[SC - OH^{-}]$ – surface trapped electron; M – organic dye pollutant.

A given material's photocatalytic performance is highly influenced by numerous factors, many of which are based on surface structures (see Figure 1-3).[40,41] The presence of these surface structures is usually due to the synthesis method and varied manipulations that are used to produce the ultimate semiconductor product. A coordinated effect occurs as these factors tend to work synchronously to potentially

generate optimal properties that can enhance the conductivity and photocatalytic performance of the material.

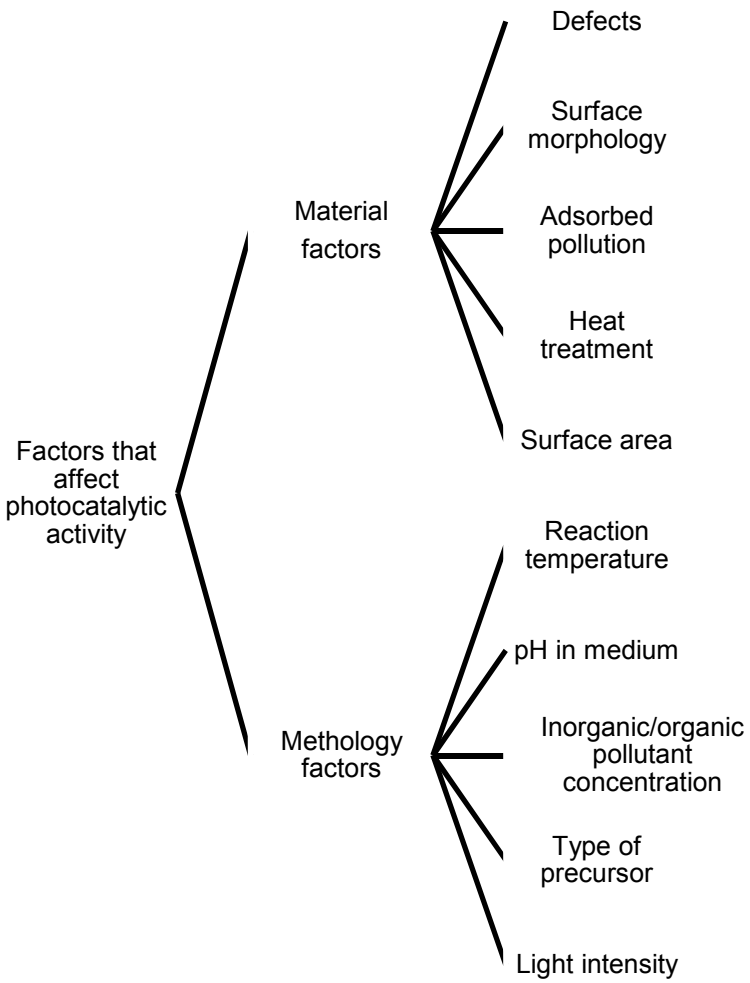

Figure 1-3 Factors that may affect the photocatalytic activity of any given semiconductor material.

1.2. Preparative Methods for Oxide Semiconductors

Over the span of five decades, numerous methods have been reported for producing semiconductor materials. Based on the synthesis method used, varied characteristic properties can exist within a material which can make them suitable candidates for specific applications. Of these methods, the conventional solid-state reaction has been the most commonly used method by researchers due to its simplicity (direct synthesis) and readily available precursors for e.g., oxides and carbonates.[42] Conversely, due to limited diffusion occurring during calcination, this process is slow to occur and employs high temperatures in excess of 1000˚C to achieve the final product. These high temperatures usually result in the formation of large particles (in the micrometer range); decomposition of the formed reaction product along with the presence of undesirable phases. Periodic grinding helps to increase product homogeneity, conversely; phase purity becomes an issue as impurities can be introduced via the reaction vessel due to continuous grinding and heat application.[43,44] Such limitations render solid state reactions to be very ineffective on the basis of time and energy efficiency.

Outside of the solid state reactions, ‘soft’, ‘mild’, or ‘wet’ chemical synthesis routes are continuously being utilized, which favor a more beneficial semiconductor product material. Hydrothermal reactions, though time consuming, utilize a low temperature (>100˚C) and high pressure (> 50 MPa) direct synthesis route.[45] The precursor materials are usually in solution and are normally placed in a closed vessel (autoclave) subjected to known temperatures and pressures for long times. Hydrothermal synthesis is quite advantageous in that the particle size and material morphology can be controlled along with improved product homogeneity.[46,47]

Sol-gel synthesis is considered a 'soft' route using low temperatures to achieve uniform products. In this method, the 'sol' is prepared by converting the respective salt precursor into a concentrated solution or a colloidal solution by adding either water or a dilute acid. Subsequent dehydration of that concentrated solution forms the 'gel'. Heat treatment of the gel in turn yields an oxide product of the salt precursor.[48] The product morphology can be controlled through process conditions (temperature, pH, etc.) with possibility of producing small particle sizes with suitable crystallinity.[49] Like many methods, sol-gel routes are time consuming due to multistep processes and they also require costly reagents.

Other methods such as electrodeposition, spray pyrolysis, chemical bath deposition, etc. have all been considered by researchers, and are continually being developed to produce many of the qualities desired in a semiconductor material.[50-54] However, solution combustion synthesis (SCS), though limited in the photocatalysis community, addresses many the above concerns. It is considered to be both a time and energy efficient process. Hence, this study focuses on this method, solution combustion synthesis (SCS) to prepare various metal-based oxide semiconductors. The next section highlights some of the key background information to further explain this process.

1.2.1. Solution Combustion Synthesis

In choosing a suitable synthesis method, consideration must be given to the time it takes for the energy needed for material synthesis to be recovered (energy payback time).[10,55] An ideal synthesis route is one that is both time and energy efficient; with a good example being combustion synthesis (CS). Combustion synthesis, also known as self-propagating high-temperature synthesis (SHS) is a process describing self-sustaining exothermic reactions that can produce quite useful materials (catalysts, composites, alloys, etc.). [56,57]

In the traditional combustion synthesis process, the starting materials e.g., nitrates or oxalates and a fuel are typically in their solid form (pressed into pellets) and made to ignite using an external source, e.g., microwave or laser. Once ignited, a high temperature wave propagates through the reaction mixture resulting in a powdered product. This exothermic process is very fast (0.1 – 10 cm s^{-1}), with high internal temperatures > 1000˚C.[58] Hence, no additional energy is required for this reaction once the mixture has ignited.

One process variant to CS is a fairly new technique called solution combustion synthesis (SCS). Similar to CS, the SCS process utilizes oxidizer (s) and organic fuel; however, the reactants are mixed in an aqueous solution instead of remaining in solid form. Metal nitrates are commonly used oxidizers because they are water soluble .The oxidizers are also the oxygen and cation sources for the reaction and the product respectively. [42,58,59] During the combustion process, the organic fuel (commonly urea) is widely exploited due to ease of availability and high exothermicity. The fuel also serves as the carbon and hydrogen source generating carbon dioxide and water and enables increased mixture homogeneity as complexes tend to form with the metal ions in solution.[43,58,59]

The overall solution combustion synthesis process occurs by mixing stoichiometric amounts of the metal nitrate and organic fuel in solution. The reaction mixture is dehydrated, ignited, and brought to combustion. The initial solution mixture allows adequate mixing of the reactants to produce particles of homogeneous and uniform composition. During the onset of the combustion reaction an exothermic propagating wave (~1000 – 1500˚C) is generated which promotes high product crystallinity.[43] The expulsion of noxious gases results in finely dispersed, porous solid particles of high purity. Short reaction times hinder particle size increase, thus favoring

nano-sized material of high surface area.[59] Additionally, there lies the possibility of incorporating 'dopants' in situ in the oxide.[10,57] Nonetheless, the SCS method is simple requiring no special equipment or expensive materials. Though relatively new in the CS field, using the solution combustion method to produce semiconductor nanoparticles has vastly increased its wide applicability for photocatalysis.[60-65]

A key component in having a successful solution combustion synthesis reaction is the stoichiometric oxidizer to fuel (O/F) ratio expressed as:[43]

$$\Phi_e = \frac{\Sigma \text{ (Coefficient of oxidizing elements) x (Valency)}}{(-1)\ \Sigma\text{(Coefficient of reducing elements) x (Valency)}} \quad (11)$$

In a given SCS reaction mixture, it is considered to be stoichiometric when $\Phi_e = 1$ (produces the maximum energy), fuel lean when $\Phi_e > 1$, and fuel rich when $\Phi_e < 1$. In determining Φ_e, the valence numbers for the oxidizing and reducing elements are done in a similar way as determining the oxidation number for chemists. For reducing elements C and H, the valence numbers are +4 and +1 respectively, while for an oxidizing element like O, the valence number is -2. Many of the metals represented as M^+, M^{2+}, and M^{3+} have valence numbers +1, +2, and +3 respectively. The SCS reaction mixtures utilized in this study exploited a stoichiometry that produced the maximum amount of energy.

Chapter 2

Band Engineering and Underlying Solid State Chemistry

2.1. Tungsten-based Oxide Semiconductors

The WO_3 monoclinic structure unit comprises of 8 W and 24 O atoms bonded in a WO_6 octahedral unit as illustrated in Figure 2-1.[66] Theoretical considerations indicate that the bottom position of the CB and the top position of the VB consist of W 5d and O 2p orbitals respectively which determine the band structure of the material. A strong crystal field strength results in WO_3 having a lower CB compared to that of TiO_2. This crystal field strength causes greater splitting of the W 5d orbital shifting the CB downward. A shift of the band edge positions can alter the energy band gap of these materials which in turn may enhance photocatalytic activity.[67] Such shift may also shrink the band gap, thus increasing solar light absorption, without changing the reduction/oxidation potential of the photogenerated charge carriers.

Introduction of a heteroatom in the WO_3 structure can result in the formation of one of two major crystal structures: wolframite (smaller divalent cations), scheelite (larger divalent cations), or other possible crystal structures (monovalent cations). Accordingly, small divalent cations (ionic radius < 0.77 Å) such as Zn and Cu tend to form wolframite structures.[68] There are many examples where newly formed binary or ternary tungstates outperformed WO_3, for example Bi_2WO_6,[69-71] $SnWO_4$,[72,73] $AgBiW_2O_8$,[60] and $AgInW_2O_8$.[74,75] Another focus of this study was to incorporate Zn, Cu, and Ag cations into the WO_3 framework to form $ZnWO_4$, $CuWO_4$, and Ag_2WO_4 respectively, thereby opening up an avenue for tuning interfacial energetics.

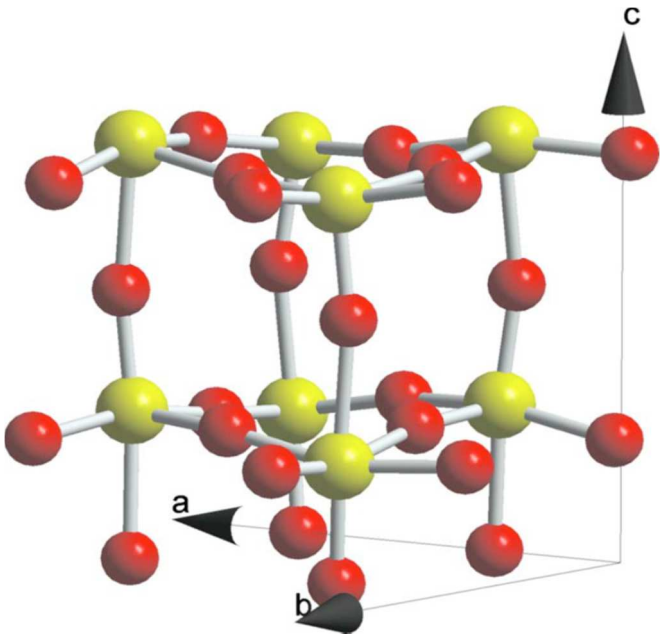

Figure 2-1 Ball and stick representation of the monoclinic WO_3 structure: tungsten – yellow balls and oxygen – red balls.

Zinc tungstate ($ZnWO_4$) crystallizes to a monoclinic wolframite structure ($P\,2/c$) with both Zn and W forming ZnO_6 and WO_6 octahedra, respectively, connected by edge sharing.[68] Copper tungstate ($CuWO_4$) crystallizes in a triclinic structure with symmetry $P\bar{1}$, with Cu and W both surrounded by six oxygen atoms to form CuO_6 and WO_6 octahedra.[76] These two different octahedra connected by edge sharing O's form infinite zigzag chains. Though triclinic, the $CuWO_4$ structure is topologically related to that of monoclinic wolframite ($P\,2/c$).[77] The CuO_6 octahedra demonstrate Jahn-Teller distortion to remove the degeneracy of Cu^{2+} 3d orbitals. This distortion elongates the octahedron causing reduction in the symmetry from monoclinic to triclinic.[78] See Figures 2-2 and 2-3 for model structure representations of zinc tungstate and copper tungstate respectively.[79]

On the other hand, introducing a monovalent cation like Ag favors a complicated network structure of silver tungstate (Ag_2WO_4) which can exhibit three different structural phases; *α*-, *β*-, or *γ*-Ag_2WO_4.[80] Among those polymorphs, *α*-Ag_2WO_4 is thermodynamically most stable belonging to orthorhombic symmetry Pn2n.[82,83] All W atoms are six-coordinate and form WO_6 octahedra. These WO_6, W_2O_6, and W_3O_6 octahedra are connected by sharing edges and grouped altogether at a particular position (see Figure 2-4). [79] Nevertheless, the number of different sites occupied by the Ag atoms in Ag_2WO_4 is six.

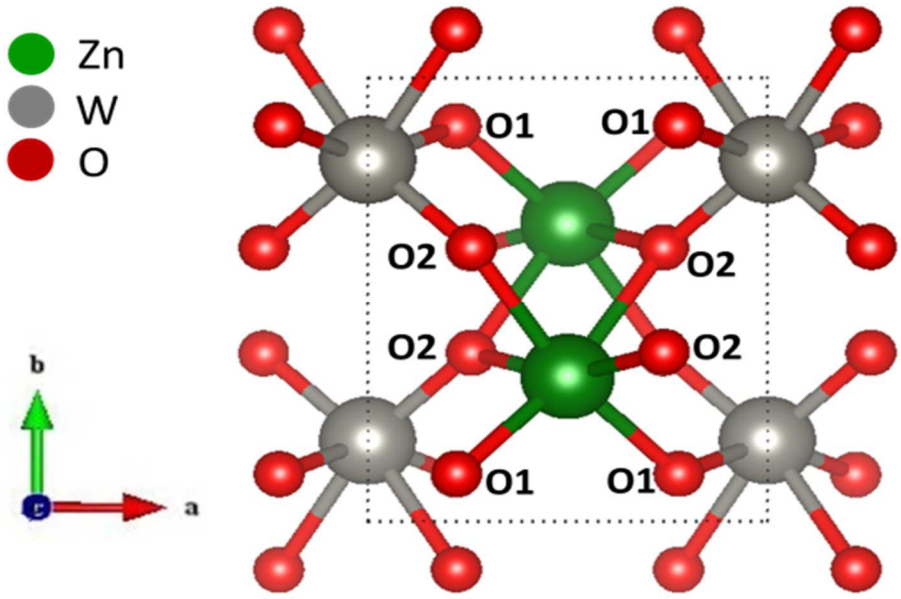

Figure 2-2 Ball and stick model of the crystal structure of $ZnWO_4$.

(Courtesy Dr. Muhammad Huda's group – Physics Department)

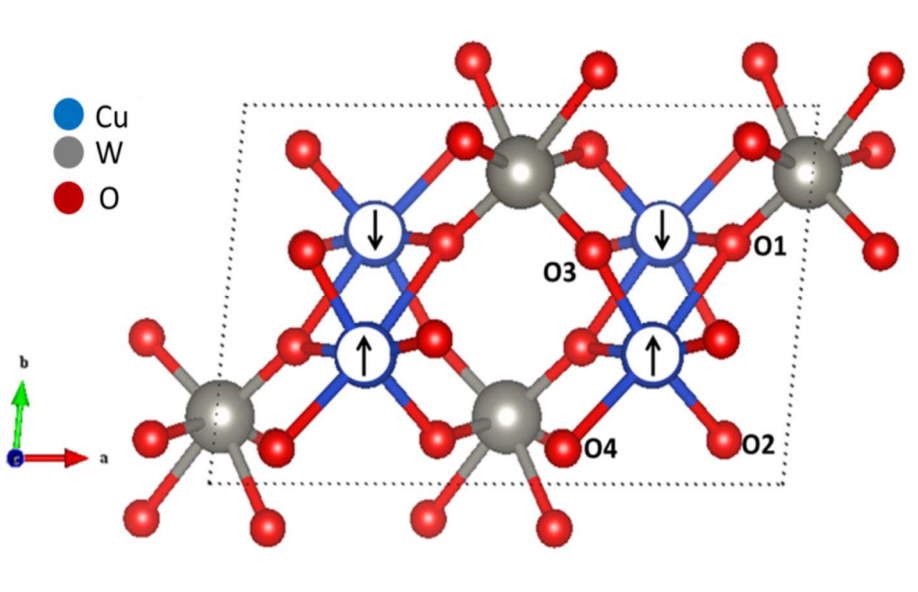

Figure 2-3 Ball and stick model of the crystal structure of $CuWO_4$.

(Courtesy Dr. Muhammad Huda's group – Physics Department)

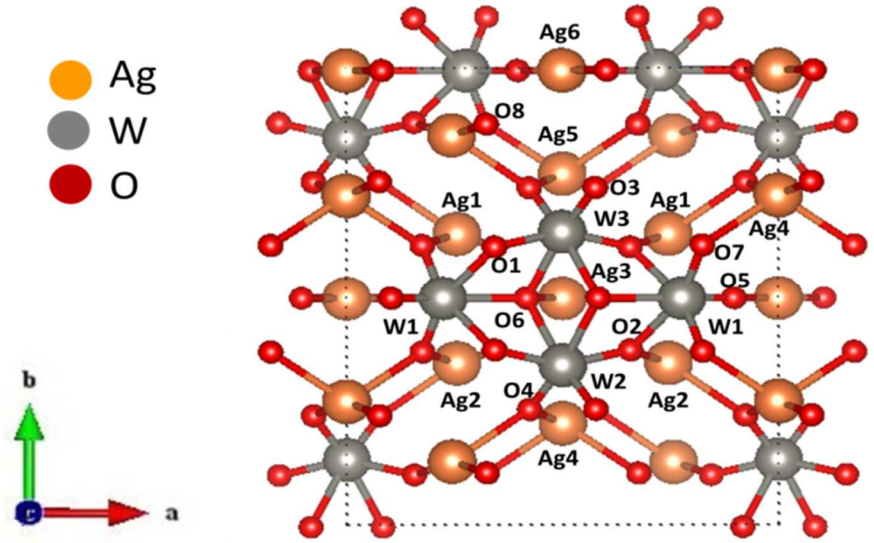

Figure 2-4 Ball and stick model of the crystal structure of Ag_2WO_4.

(Courtesy Dr. Muhammad Huda's group – Physics Department)

As suggested, the insertion of these different metals in WO_3 does give rise to changes in the band edge positions, see Figure 2-5. In $ZnWO_4$, the W 5d CB shifts upward to a more negative potential owing to a longer bond length and weaker crystal field strength in the WO_6 octahedra. Its VB (Zn 3d + O 2p) remains fairly close to that of WO_3.[68] In $CuWO_4$ the W 5d orbital remains unchanged, however, the VB shifts upward due to the hybridization of the Cu 3d and O 2p orbital resulting in a lower E_g than WO_3.[82] Like $ZnWO_4$, Ag_2WO_4 has a weak crystal field strength resulting in the W 5d CB shifting upwards compared to WO_3.[83,84] The positive VB that exists for the proposed W-based oxide semiconductors make them suitable materials for photo-oxidation reactions. $CuWO_4$, with a more positive CB is not ideal for photo-reduction reactions; however, the upward shifting of the W 5d CB makes $ZnWO_4$ and Ag_2WO_4 eminently attractive candidate photocatalysts for such a process.

Literature survey indicates that synthesis of $ZnWO_4$, $CuWO_4$, and Ag_2WO_4 has been dominated by conventional methods such as solid state reaction and hydrothermal synthesis.[68,83,85-89] Other methods include: sol-gel reaction, spray deposition, electrochemical deposition, mechanochemical synthesis, precipitation, and top-seeded solution growth.[78, 90-97] These methods suffer from similar drawbacks including long reaction times and high energy input to sustain the reaction process.

Furthermore, there have been no reports on the use of the solution combustion synthesis method to produce this selected family of tungstates. Hence, this study utilized this novel method of synthesis to prepare $ZnWO_4$, $CuWO_4$, and Ag_2WO_4. The influence of the precursor on each product's structural attributes and morphology was assessed by using two different tungsten based precursors in the synthesis process. Moreover, each material's photocatalytic activity was evaluated for its ability to degrade an organic

pollutant methyl orange dye and later comparing the apparent rate constants with its commercially available counterparts.

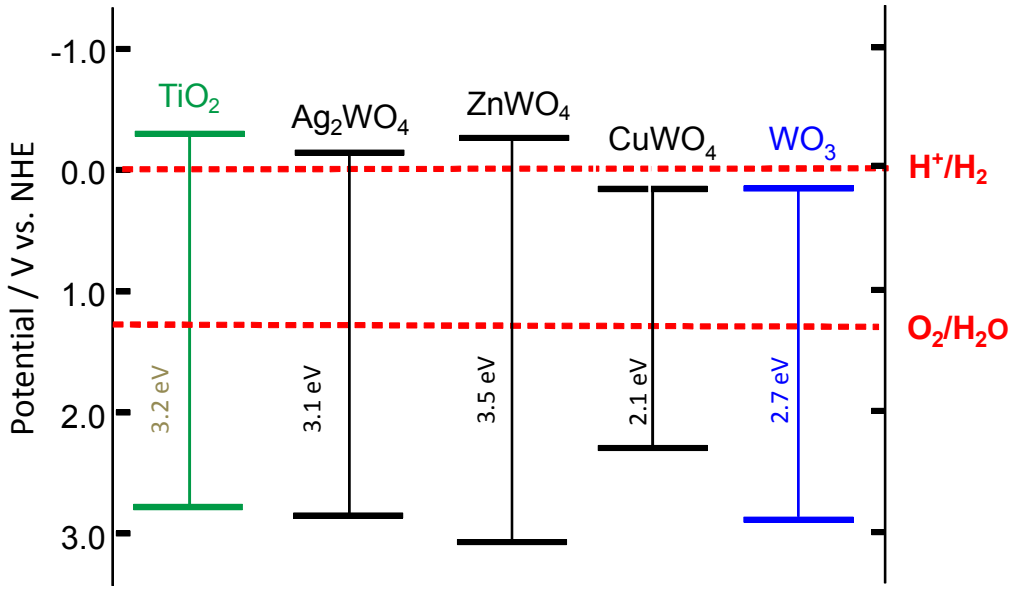

Figure 2-5 Schematic representation of approximate conduction and valence band edge positions of the binary tungsten-based oxides. The interfacial energetics for TiO_2 and WO_3 are also shown for comparison.

2.2. Niobium-based Oxide Semiconductors

Transition metal niobium-based oxide semiconductor materials have been widely explored as they possess excellent magnetic and dielectric properties.[98-101] Many of these materials are binary niobates conforming to the formula $M^{2+}Nb_2O_6$, where M^{2+} = 2+

cations (Zn, Cu, Co, Ni, Mn, etc.) with < 1.0 Å ionic radii and have an orthorhombic columbite structure.[98,102]

Zinc niobate ($ZnNb_2O_6$) commonly crystallizes to an orthorhombic structure with space group *Pbcn*/Pnab, while $CuNb_2O_6$ exhibits two polymorphs: a monoclinic (*P2/c*) and an orthorhombic $CuNb_2O_6$ crystal structure.[98,103] In fact, literature survey shows the formation of these two $CuNb_2O_6$ polymorphs at different reaction temperatures. That is, the monoclinic $CuNb_2O_6$ can be obtained at temperatures < 740˚C, while the orthorhombic form is formed at temperatures > 740˚C.[103-105] Most recently, materials aside from the known stoichiometry of $ZnNb_2O_6$ and $CuNb_2O_6$ are being developed with varying phases. The introduction of these newly synthesized materials allows for the tuning of bandgap energies, making them applicable for photocatalytic and photoelectrochemical processes.[106-111]

Within the $ZnNb_2O_6$ and $CuNb_2O_6$ structure, Zn:Nb and Cu:Nb are each surrounded by six oxygen atoms which form zig-zag chains of ZnO_6:NbO_6 and CuO_6:NbO_6 octahedra connected by edge sharing. These zig-zag chains in turn are connected by corner sharing, creating an ordered repeating *M* – NbO_6 – NbO_6 – *M* – NbO_6 – NbO_6 – *M* octahedral layers, where M = ZnO_6 or CuO_6 in $ZnNb_2O_6$ and $CuNb_2O_6$ respectively.[98,102] See Figures 2-6 and 2-7 for the model structure representation of these binary niobates. To date, solid state reactions (high temperature process) have predominantly been the method of choice for synthesizing these transition-metal niobates as they are easily made from simple metal oxides.[103,112,113] However, the last two decades have experienced an increased momentum on utilizing lower temperature synthesis techniques like sol-gel method, co-precipitation, and hydrothermal method to prepare these niobates.[114-117] These methods along with the solid state reactions are time and energy inefficient as mentioned earlier.

Therefore, this study is focused on $ZnNb_2O_6$ and $CuNb_2O_6$ prepared by a novel method: solution combustion synthesis, with keen attention on the material's crystal structure formation and morphology. Additionally, photoelectrochemical investigations were done on the materials to evaluate their characteristic properties as well as their ability for CO_2 reduction.

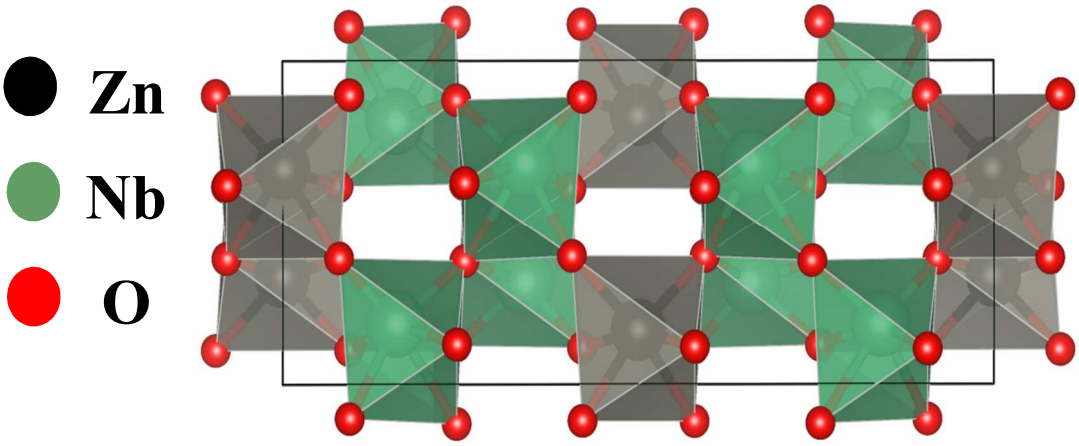

Figure 2-6 Polyhedral model of the crystal structure for $ZnNb_2O_6$.

(Courtesy Dr. Muhammad Huda's group – Physics Department)

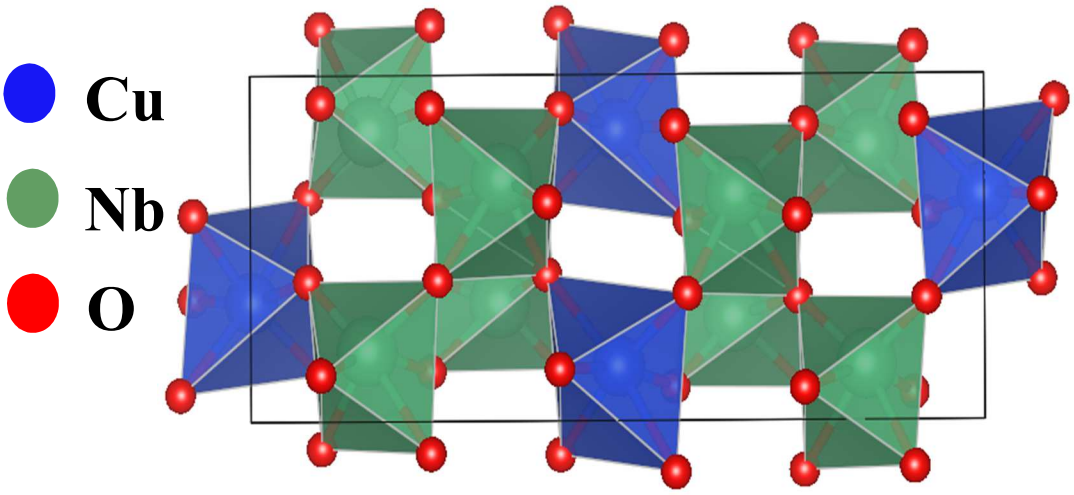

Figure 2-7 Polyhedral model of the crystal structure for $CuNb_2O_6$.

(Courtesy Dr. Muhammad Huda's group – Physics Department)

Chapter 3

Preparative Methods and Materials Characterization

3.1. Tungsten-based Oxide Semiconductors

3.1.1. Materials

Zinc nitrate hexahydrate – $Zn(NO_3)_2 \cdot 6H_2O$ (Alfa Aesar), copper (II) nitrate hemihydrate – $Cu(NO_3)_2 \cdot 2.5H_2O$ (Alfa Aesar), and silver nitrate – $AgNO_3$ (Fisher) were used as the zinc, copper, and silver precursors respectively. Sodium tungsten oxide dihydrate – $Na_2WO_4 \cdot 2H_2O$ (Alfa Aesar) and ammonium tungsten oxide – $(NH_4)_2WO_4$ (Alfa Aesar) were used as the tungsten precursors and urea as the fuel. All chemicals were used without further purification. Double distilled water (Corning Megapure) was used to prepare all solutions. Commercial samples of $ZnWO_4$, $CuWO_4$, and Ag_2WO_4 (all Alfa Aesar) were used as reference materials for benchmarking the characteristics of the combustion synthesized nanopowders.

3.1.2. Solution Combustion Synthesis

Stoichiometric amounts of the respective metal nitrate, sodium tungstate precursor, and fuel were placed in a crucible and homogenized in double distilled water. The solution mixture was then transferred to a preheated furnace at 350˚C and left for 5 min. This allows for dehydration of the precursor mixture and the promotion of spontaneous combustion. As for ammonium tungstate, it was first homogenized in 1.5 M HNO_3 medium and then placed in a crucible with the metal nitrate precursor and fuel solution. The solution was placed in a preheated furnace at 350˚C and left for 5 min.

Once the SCS process was completed, the samples were removed, finely ground in a mortar and pestle, and thermally annealed at temperatures 400˚C, 450˚C, and 500˚C for 30 min. Thereafter, each sample (both as-synthesized and heat treated) was washed

with double distilled water to remove any soluble residues coming from the precursor species, filtered, and dried in an oven at 100˚C.

Table 3-1 Synthesized samples prepared from different tungsten precursors.

Sample	Metal precursor	Tungsten precursor	Fuel
$ZnWO_4$ (Na)	$Zn(NO_3)_2 \cdot 6H_2O$	$Na_2WO_4 \cdot 2H_2O$	Urea
$CuWO_4$ (Na)	$Cu(NO_3)_2 \cdot 2.5H_2O$		
Ag_2WO_4 (Na)	$AgNO_3$		
$ZnWO_4$ (NH_4)	$Zn(NO_3)_2 \cdot 6H_2O$	$(NH_4)_2WO_4$	
$CuWO_4$ (NH_4)	$Cu(NO_3)_2 \cdot 2.5H_2O$		
Ag_2WO_4 (NH_4)	$AgNO_3$		

3.2. Niobium-based oxide semiconductors

3.2.1. Materials

Zinc nitrate hexahydrate – $Zn(NO_3)_2 \cdot 6H_2O$ (Alfa Aesar), copper nitrate – $Cu(NO_3)_2 \cdot 2.5H_2O$ (Alfa Aesar), ammonium niobium oxalate hydrate – $NH_4[NbO(C_2O_4)_2] \cdot 2H_2O$ (Sigma Aldrich), niobium pentoxide – Nb_2O_5 (Sigma Aldrich), were used as the cation sources and oxidizers in the reaction, and urea as the fuel. All materials were used as received. Double distilled water (Corning Megapure) was used to prepare all solutions. Commercially available samples (Sigma Aldrich) were used for benchmarking the solution combustion synthesized materials.

3.2.2. Solution Combustion Synthesis

The respective metal nitrate, niobium precursor, and urea of stoichiometric quantities were measured and dissolved in double distilled water. Each solution was placed in individual crucibles and placed in a preheated furnace at 350°C. The resultant products were removed, finely ground in a mortar and pestle and then annealed at 600°C. Once complete, samples were washed, filtered and dried in an oven at 100°C. Figure 3-1 shows a flowchart of the overall solution combustion synthesis reaction procedure.

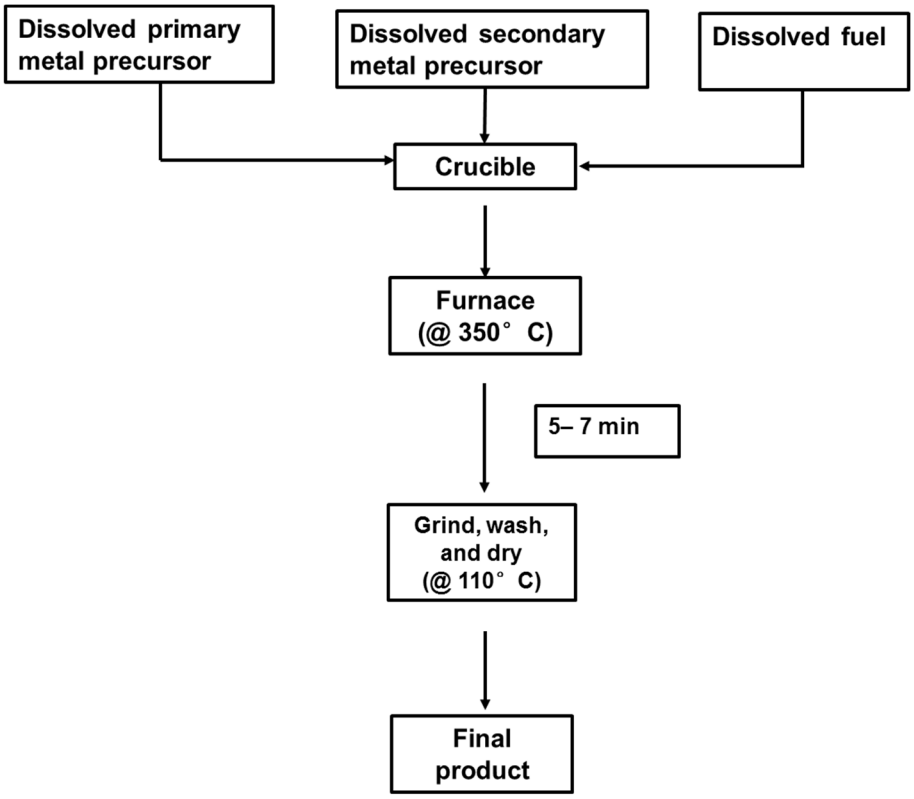

Figure 3-1 Flowchart of the solution combustion synthesis reaction procedure.

3.3. Physical Characterization Techniques

Characterization of the solution combustion synthesized materials was done by various methods mainly associated with materials science. Techniques such as XRD, TEM, and Raman spectroscopy are commonly used when studying material morphology, which plays a key role in the materials capabilities for good photocatalytic performance. In order to gain a deeper insight into the different characterization techniques used, a brief overview of each one is described below.

3.3.1. Thermogravimetric Analysis (TGA)[118]

Thermogravimetric analysis (TGA) is a technique that measures mass changes of a desired material as a function of temperature or time under a controlled atmosphere. A plot of mass percentage against temperature can enable the interpretation of mass loss curve transformations; for example, by finding the points where rapid mass loss occurs. Such a method can be employed to simulate reaction processes by using precursor materials under appropriate temperature and gaseous conditions. Also, a better understanding of total thermal decomposition of the precursor materials can be attained via data interpretation. Furthermore, quantitative information can be obtained about thermal oxidative stability of newly formed products and physical processes such as vaporization and sublimation.

3.3.2. Differential Scanning Calorimetry (DSC)[118,119]

Differential scanning calorimetry (DSC), usually done in conjunction with TGA, measures the rate of change of heat flow within a material and reference as a function of temperature (temperature scan mode). The data retrieved can yield both quantitative and qualitative information on physical and chemical changes occurring within a material. These changes include exothermic/endothermic processes, crystallization behavior, heat of reactions, reaction kinetics, as well as thermal stability.

To model the SCS procedure, thermogravimetric analysis/differential scanning calorimetry (TGA/DSC) analyses on the precursor mixtures were carried out using a TA Instruments model Q600 instrument. The precursor mixture was placed in an alumina crucible in air atmosphere with a flow rate of 100 mL/min and heated at 10°C/min up to 1000 °C.

3.3.3. X-ray Diffraction (XRD)[120,121]

X-ray diffraction is a non-destructive characterization technique ideal for studying the crystal structure, crystallite size, and chemical composition of a material (both polycrystalline and single crystal samples). Powder X-ray diffraction is highlighted here as powdered semiconductor materials are the focus of this study. In the powder x-ray diffraction process, a convergent incident beam is directed at the material where its electrons collide with the photons from the incident beam causing diffractions. These beams are diffracted at many angles due to the many crystalline planes present in the material according to Bragg's law:

$$n\lambda = 2d \sin \theta \quad (12)$$

where n is an integer, λ is the wavelength of the x-ray beam, d is the spacing between the atomic planes in the crystalline phase, and θ is the diffraction angle. Thereafter, the x-ray detector rotates in a circular motion recording all the diffraction angles and intensity which can then be digitally reported.

From the recorded intensity and diffraction angles, the average crystallite size of the material can be calculated using the Scherrer equation:

$$D = K \lambda / \beta \cos\Theta \quad (13)$$

where D is the particle size, K is a constant (0.89 – 1.0), λ is the CuK_α wavelength (1.5405 Å), β is the full-width-at-half-maximum (FWHM) in radians of a selected diffraction peak, and θ is the diffraction angle.

Powder X-ray diffraction (XRD) measurements were performed within the angle range 2θ = 10 - 80° using a Rigaku Ultima IV with a Cu Kα radiation source (λ=1.5406). Rietveld refinements were carried out on MDI Jade 8 software, using initial model structures from reported literature. Refinements were also performed on each of the samples with reduced scale and background parameters and individual FWHM (full width half maximum) curves to account for all the peaks in the XRD pattern. The peak shapes were fitted using the Gaussian profile function with a displacement option used allowing for any deviations from the model structure.

3.3.4. Diffuse Reflectance Spectroscopy[122]

Diffuse reflectance measurements of various semiconductor materials are commonly obtained using a UV-visible spectrophotometer. Such measurements are quite useful in estimating the band gap energy (band gap) and the absorption coefficient of a powdered sample with minimum preparation. The diffuse reflectance measurement process requires the use of a small amount of powdered sample with thickness ranging from 1 – 3 mm. This thickness ensures adequate absorption and scattering of the incident light before it reaches the back surface of the sample holder. Powdered samples are usually measured by this method owing to numerous surfaces that can scatter and absorb light. The band gap energy is routinely estimated by generating Tauc plots, i.e., plotting $(\alpha h\nu)^n$ vs photon energy ($h\nu$), where α (also represented by k) is the absorption coefficient. Optical transitions that exist for the material is represented by n; where n = 2 is a direct transition and n = ½ is an indirect transition. The Kubelka – Munk model enables a quantitative assessment of the reflectance from a layer that scatters and absorbs light. Represented below in equation 14 is the Kubelka – Munk function.

$$f(R'_\infty) = \frac{(1 - R'_\infty)^2}{2R'_\infty} = \frac{k}{s} \qquad (14)$$

where R' is the ratio of the reflected intensity of the sample to that of a non-absorbing standard, e.g., potassium chloride or barium sulfate, *k* the molar absorption coefficient of the analyte, and *s* the scattering coefficient.

The UV-visible diffuse reflectance spectra were collected on a Perkin Elmer Lambda 35 spectrophotometer equipped with an integrating sphere. Thereafter, the band gap energies were estimated by generating Tauc plots.[122]

3.3.5. Raman Spectroscopy[120]

Raman spectroscopy is a quantitative and qualitative technique based on the inelastic scattering of light. It is very useful for identifying unknown compounds in solution, powders, polycrystalline solids, and thin films. A given material is usually irradiated by monochromatic light resulting in the vibration of molecules and the scattering of light. Light interaction with the material molecules can result in the reduction of photon energy (Stokes shift) while excited atoms in the material can relax transmitting energy back to the incident light having more energy (anti-Stokes shift). Stokes Raman shift, though usually weak, is of most importance for the production of a Raman spectrum.

Raman spectra were obtained from a Horiba Jobin Yvon Labram Aramis spectrometer at an excitation wavelength of 633 nm, using a He-Ne laser by averaging 64 spectra.

3.3.6. Electron Microscopy (SEM and TEM)[120,121]

Electron microscopy reports on the distribution of grains and defects present within the material along with surface characteristics. In acquiring a suitable image, the sample should be relatively thin to allow for maximum intensity from the transmitted beam of electrons. For SEM analysis, the initial preparation requires that small amounts of each sample are dispersed in isopropanol; drop-cast on a stainless steel substrate and then

dried. Thereafter, the morphology of the sample was analyzed using a Hitachi S4800 FESEM. Similar preparations were done to samples for TEM imaging. Before the actual analysis process, small amounts of the sample (few mg) were dispersed in isopropanol and sonicated for approximately an hour and then a fine grid was dipped into the particle solution and left to dry. High resolution transmission electron microscopy (HR – TEM) was performed on a Hitachi H – 9500 instrument at various magnifications.

3.3.7. Computational Details

The calculations were performed by Mr. Pranab Sarker in Dr. Huda's group of the Physics Department at The University of Texas at Arlington.

The calculations were performed within the framework of the standard frozen-core projector augmented-wave (PAW) method[123,124] using DFT as implemented in Vienna ab initio simulation package (VASP 4.6) code.[125,126] In the PAW method, a non-linear core-correction is not necessary because it is an all-electron-like method. Exchange and correlation potentials were treated in the generalized gradient approximation (GGA) as parameterized by Perdew-Burke-Ernzerhof (PBE).[127,128] The PBE functional does not contain any empirically optimized parameters, and hence works better on a wide range of elements. It is well known that underestimation of electron localization is a major failure of standard DFT calculations, in particular, for systems with localized d and f electrons.[129-131] This failure manifests the general trend of DFT to underestimate the band gap and to produce incorrect solutions for some 3d based metal oxides. In order to correct this shortcoming, an on-site Coulomb correlation was employed through the Hubbard-based U correction parameter.[131-133]

For the tungstate materials, U = 7eV was used that externally provides Coulomb correlation to only Cu 3d and Zn 3d orbitals. Hence, all results presented here are based on DFT+U calculation for both $ZnWO_4$ and $CuWO_4$ and DFT calculation for Ag_2WO_4. The

basis sets were expanded with plane-waves with a kinetic energy cut-off of 400 eV, and BZ integrations were performed using the second-order Methfessel-Paxton method.[134] The optimization of $ZnWO_4$, $CuWO_4$, and Ag_2WO_4 structures were done using 11×9×11, 5×9×9, and 5×5×9 Monkhorst–Pack k-point sampling.[135] However, more refined 9×13×13, 15×13×15, and 7×7×11, k-point samplings were used for $ZnWO_4$, $CuWO_4$, and Ag_2WO_4 respectively for optical properties calculations.

For the niobate samples, U_{eff} = 6 eV (U_{eff} = U-J = 7-1 = 6 eV, J = Stoner exchange parameter) was used that externally provides Coulomb correlation to both Cu 3d and Zn 3d orbitals in Cu- and Zn-niobates, respectively. This value of U_{eff} was chosen from previous work on Cu and Zn based compounds.[79,136-138] The basis sets were expanded with plane-waves with a kinetic energy cut-off of 400 eV. The ion positions and volumes were always relaxed without any symmetry constraint to allow the internal geometry and the shape of the lattice to be changed freely until the force on each of the ion was 0.01 eV/Å or less. The optical absorption calculation of MNb_2O_6, (M = Cu and Zn) used 9×3×7 Monkhorst–Pack k-point sampling. [135] The BZ integrations were performed using the second-order Methfessel-Paxton method.[134]

For visualization of the crystal structures, VESTA (Visualization for Electronic and Structural Analysis) was used.[139,140] Calculations were performed by Dr. Huda's group at the High Performance Computing (HPC) Center at the University of Texas at Arlington.

3.4. Semiconductor Application Processes

3.4.1. Photocatalytic Analysis

The photocatalytic activity of the various nanoparticles was evaluated by their ability to degrade methyl orange (MO) as a probe dye in aqueous solution. A photocatalytic reactor consisting of an outer cylindrical glass vessel (400–700 nm transmittance) and an interchangeable quartz/glass inner vessel was used for the

photocatalysis process. The light source, a 400 W medium pressure Hg arc (incident photon flux estimated by potassium ferrioxalate actinometry was 5.21×10^{-4} Einsteins per minute), placed in the inner vessel, was also equipped for water circulation aimed at maintaining a constant reactor temperature, as well as for filtering infrared radiation. The outer reaction vessel was equipped with a sample collection port, in addition to a gas purge connection and a stirrer to ensure dispersion of the mixture and to prevent the catalyst from sedimentation. Figure 3-2 illustrates the photocatalysis reactor used for this analysis.

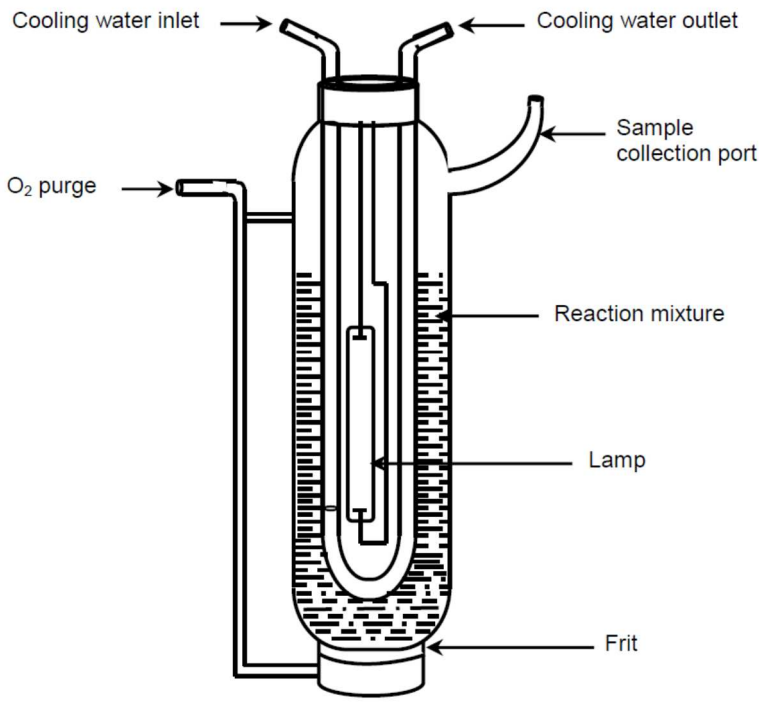

Figure 3-2 Diagram of the photocatalytic reactor utilized with powder semiconductor materials.

Testing of the photocatalytic activity was carried out using a 250 mL MO (50 μM) reaction solution along with the photocatalyst (dose: 2 g L^{-1}) while being purged with O_2 gas. The reaction suspension was initially stirred in the dark for 60 min to attain adsorption equilibrium of MO on the catalyst surface. After 60 min, the solution was irradiated with UV-visible light. Sample aliquots of 5 mL were periodically removed from the outer vessel every 10 min with the suspension being centrifuged and filtered (0.45 μm PVDF membrane filter) to remove the photocatalyst powder. The extent of MO degradation was assessed by measuring the absorbance of the solution using an Agilent 8453 UV-visible spectrophotometer. Blank runs were performed under identical experimental conditions without the photocatalyst.

3.4.2. Liquid Chromatography – Mass Spectrometry (LC-MS)

All the LC-MS measurements were performed by Ms. Evelyn Wang in Dr. Schug's group – Chemistry & Biochemistry Department at the University of Texas at Arlington.

The photocatalytic process was monitored by LC-MS analyses, performed on a Shimadzu LCMS-ITTOF (ion trap – time-of-flight) mass spectrometer (Shimadzu Scientific Instruments, Inc., Columbia MD).[141] Samples were taken from the reaction vessel at different times (t = 0, 10, 20, 30, 40, 50, 60, 70, and 80 min) during the reaction and were analyzed to determine the degradation of methyl orange and the formation of intermediates and products. 30 μL of sample was injected onto a reverse-phase column (Raptor C18, 2.1× 100 mm; 2.7 μm, Restek Corporation, Bellefonte, PA, USA) and binary pumps carrying mobile phase of 10 mM ammonium acetate or 0.1% formic acid and acetonitrile with a flow rate of 0.3 mL/min were used to obtain separation for scouting purposes. A 10 min gradient was developed with 5-99% acetonitrile followed by the washing and equilibrating steps. The eluent entered the electrospray ionization (ESI)

interface, which was operated in either positive or negative ionization mode. Interface voltages for positive or negative ionization modes were + 4.50 kV or - 4.00 kV, respectively. Mass range was set to record from 100-500 m/z. The curved desolvation transfer line and heat block temperatures were both set at 200° C. Nebulizing gas (nitrogen) was flowed at 1.5 L/min, and the detector voltage was set at 1.64 kV.

MS^2 was performed to identify the major intermediates formed during the photocatalytic reaction. Precursor ion isolation width was set at 3.0000 Da with 10 ms ion accumulation time. Collision energy was at 27% and collision gas was at 50% with a frequency of 45.0 kHz. MS^2 measurements were carried out by Ms. Evelyn Wang of Dr. Shug's group at the University of Texas at Arlington.

3.5. Photoelectrochemistry

The photoelectrochemical measurements were carried out by Dr. Csaba Janaky's group – Department of Physical Chemistry and Material Science at The University of Szeged.

All electrochemical measurements for the tungstate and niobate materials were performed on an Autolab PGSTAT302 instrument, in a classical one-compartment, three-electrode electrochemical cell. Various tungstate and niobate nanoparticles were spray coated on ITO glass electrodes (~0.1 mg cm^{-2}) and were used as working electrodes. A large Pt foil counterelectrode and an Ag/AgCl/3M KCl reference electrode completed the cell setup. The light source was a 300 W Hg-Xe arc lamp (Hamamatsu L8251). The radiation source was placed 2 cm away from the working electrode surface. Photovoltammetry profiles were recorded in both 0.1 M Na_2SO_3 and 0.1 M Na_2SO_4 electrolyte, using a slow potential sweep (2 mV s^{-1}) in conjunction with interrupted irradiation (0.1 Hz) on the semiconductor coated electrodes. All procedures were performed at the laboratory ambient temperature (20 ± 2 °C).

Chapter 4

Results and Discussion

4.1. Tungsten-based Oxide Semiconductors[80]

4.1.1. Thermogravimetric analysis

The use of thermal analysis can give a better understanding of the SCS process. Hence, for the simulation of the SCS procedure, TGA/DSC measurements were carried out on each of the precursor mixture. As an example, TGA and DSC profiles for the formation of $CuWO_4$ from two different precursor mixtures are given in Figures 4-1 and 4-2. The tungstate samples made with both precursors showed multiple mass loss regimes. The initial mass loss between 100–150˚C corresponds to the loss of water from the precursor mixture in both cases. Using the ammonium tungstate precursor, all subsequent mass loss occurs in one single step above 300˚C, originating from the combinations of fuel and metal salt precursor decomposition (and combustion). Note however, that the above mentioned temperature is only the temperature where the combustion initiates, the actual temperatures attained during combustion can be much higher than those indicated on the x-axis (given by the programmed temperature ramp, see experimental details). On the other hand, samples made with the sodium tungstate precursor, had an expanded temperature range of 120–210˚C assigned to the decomposition of the fuel and the metal salt precursor. At temperatures over 480˚C another mass loss regime was observed corresponding to the loss of residual carbon in the matrix.

Quantitative assessment of the TGA curves was also performed (Figure 4-1). As the first step, the initial mass loss (related to water evaporation) was subtracted. Subsequently, the relative mass losses were determined for both mixtures and these values were compared with the theoretically calculated values. The good agreement

between the actual and stoichiometric mass losses for both the sodium (34% vs. 31%) and the ammonium precursor (39% vs. 41%) confirmed that the proposed combustion reaction occurs in both cases, albeit with different intensity.

DSC analysis yielded both endothermic and exothermic peaks (Figure 4-2). A fairly large and broad endothermic peak was witnessed at the early stage of analysis assignable to the initial loss of moisture within the precursor material and correlating with the first mass loss on the corresponding TGA profile. More intense and sharp exothermic peaks were observed for the precursor mixtures containing $(NH_4)_2WO_4$, compared to those with Na_2WO_4 (Figure 4-2), perhaps not surprisingly in light of its combustible N-content. This exothermic peak suggests that a high combustion temperature is reached during the reaction, also coinciding with the oxidative decomposition of the fuel.

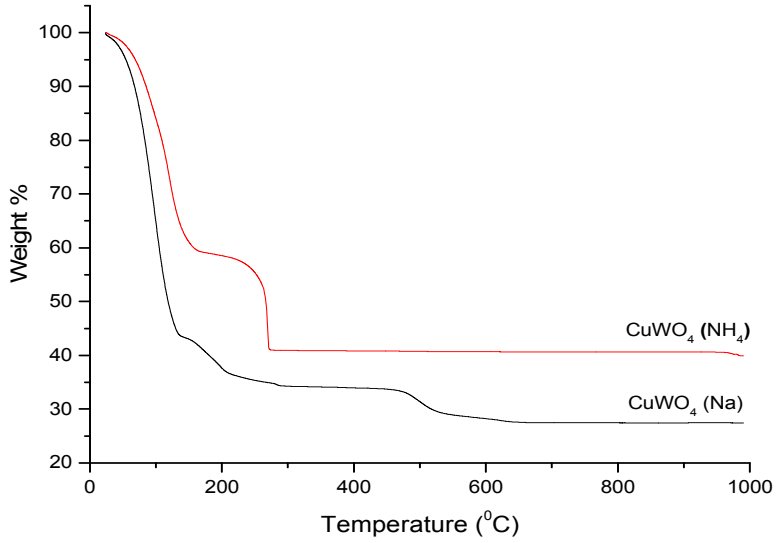

Figure 4-1 TGA profiles of the SCS precursor mixtures for $CuWO_4$.

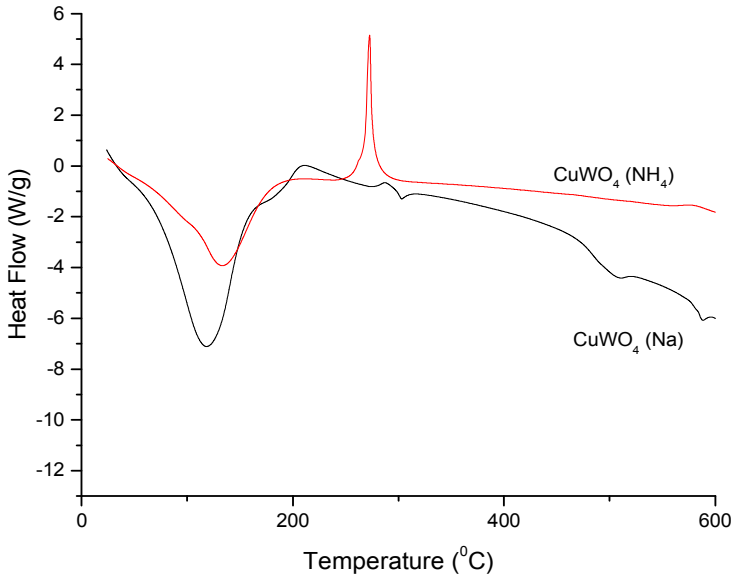

Figure 4-2 DSC profiles of the SCS precursor mixtures for $CuWO_4$.

4.1.2. Crystal Structure and Morphology

Powder X-ray diffraction was employed to characterize the crystalline phases of the synthesized and respective commercial oxide samples. The as-synthesized materials made with different tungstate precursors were annealed at varying temperatures up to 500˚C (except for $CuWO_4$, where the maximum temperature was 400˚C) to enhance the degree of crystallinity and to remove any carbon residue and impurities that may be present. Figures 4-3 – 4-5 illustrate the XRD patterns mapping the changes in the sample crystallinity from as – synthesized to the sample annealed at the highest temperature. The various oxides and more interestingly even the same oxide synthesized using different precursors show distinctly different purity and degree of crystallinity. Therefore

careful Rietveld refinement was performed on the XRD data obtained at the highest anneal temperature.

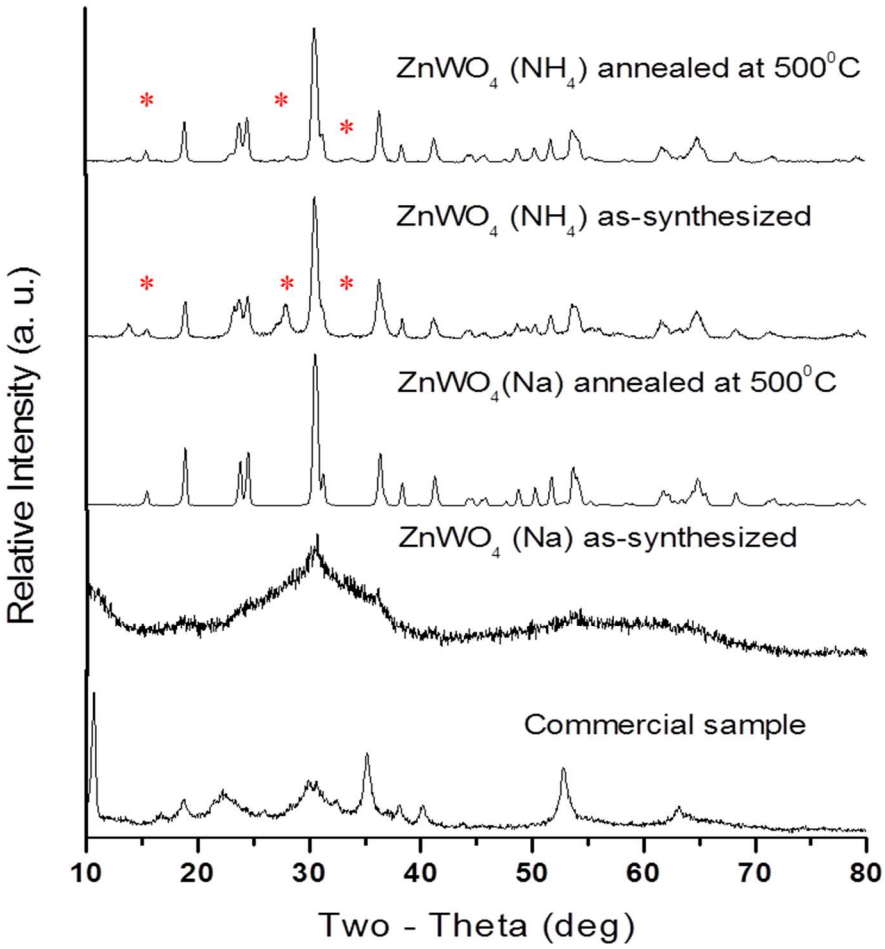

Figure 4-3 XRD patterns for $ZnWO_4$ samples. (*) represents the presence of the WO_{3-x} in the synthesized samples.

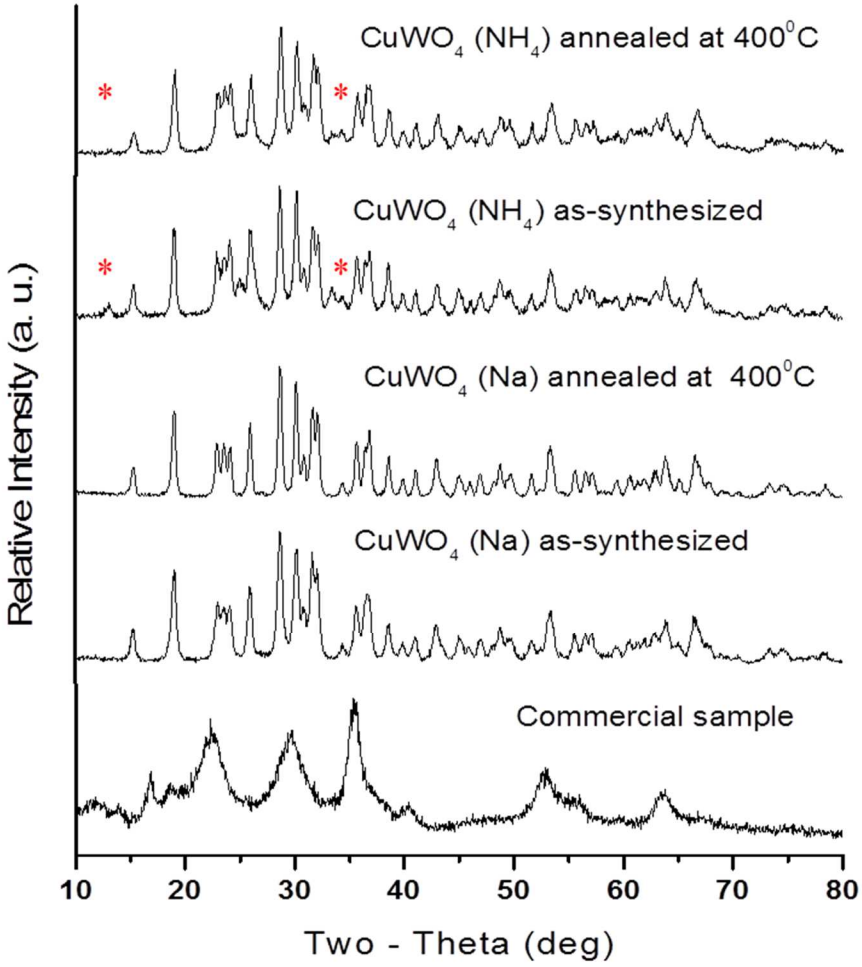

Figure 4-4 XRD patterns for $CuWO_4$ samples. (*) represents the presence of the WO_{3-x} in the synthesized samples.

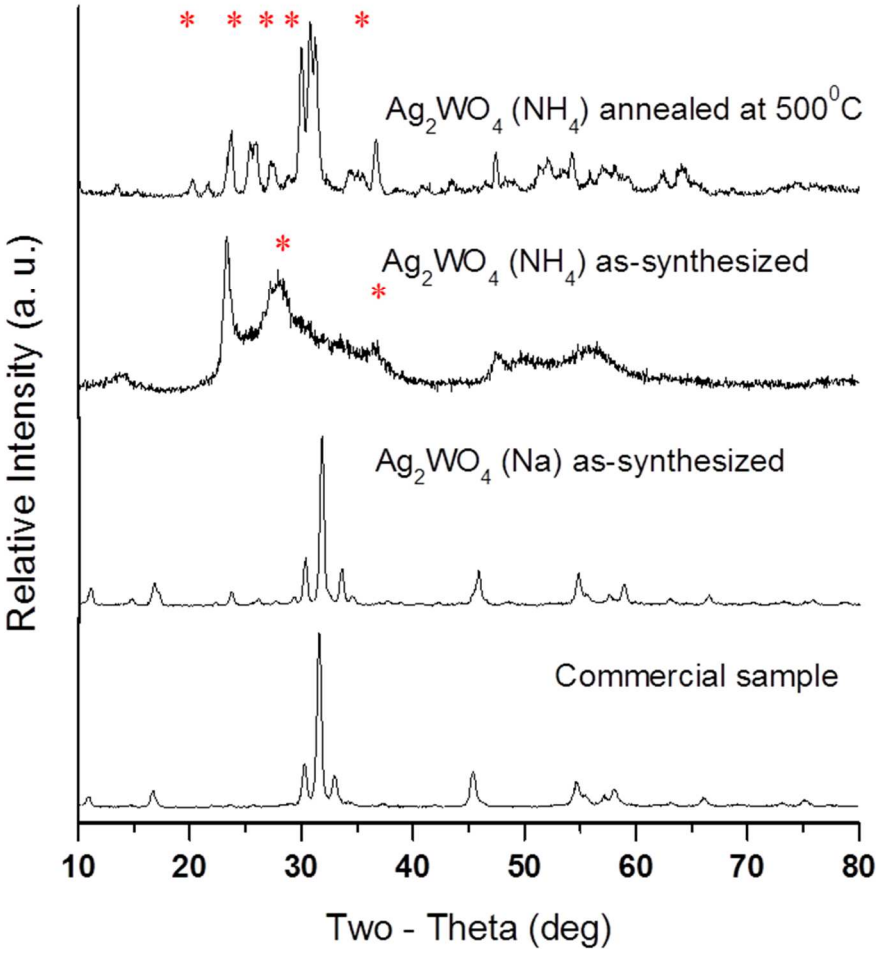

Figure 4-5 XRD patterns for Ag_2WO_4 samples. (*) represents the presence of the WO_{3-x} in the synthesized samples.

Detailed analysis of the XRD patterns presented above are given in what follows. In Figure 4-3, the as-synthesized $ZnWO_4$ (Na) sample is seen to have a high degree of amorphous phase. However, at the highest anneal temperature (500˚C), the crystalline

nature of the sample vastly improved. Rietveld refinement indicated a pure single phase monoclinic structure, *P 2/c*, with a goodness of fit (χ^2) of 1.26. This obtained pattern was in full agreement with the $ZnWO_4$ standard JCPDS file and the DFT + U calculations. XRD patterns of the $ZnWO_4$ (NH_4) sample yielded sharp peaks even from initial synthesis. This increased crystallinity, even for the as-synthesized sample, can be attributed to the reaction exothermicity brought on by the use of nitrogen-containing tungstate precursor (See Figure 4-2, the DSC profiles shown before). However, Rietveld refinement determined the presence of $ZnWO_4$ and WO_3 as the major and minor phases respectively. The χ^2 value was found to be 1.6. Additionally, what is indeed surprising, the commercial sample was not of a single phase, and exhibited a low degree of crystallinity with a χ^2 value of 2.97 with the majority $ZnWO_4$ (53.8%) and minority WO_3 (46.2%) present.

For both $CuWO_4$ samples, XRD patterns showed a high degree of crystallinity even before annealing, highlighting the beneficial features of the SCS procedure. Although both samples are in crystalline form, a single phase, triclinic structure (JCPDS No. 01-080-1918) with a χ^2 of 1.26 was determined via Rietveld analysis for the $CuWO_4$ (Na) sample. This experimental result also coincided with DFT + U calculations. A χ^2 of 1.22 resulted for the $CuWO_4$ (NH_4) sample; however, like $ZnWO_4$ (NH_4), multiple phases were present in this sample with $CuWO_4$ and $W_{17}O_{47}$ as the major and minor phases respectively. The commercial sample was fairly crystalline; it too contained multiple phases with a 79.1% $CuWO_4$ majority. Both samples showed the presence of peaks that did not conform to any known phases with increasing anneal temperatures. Additionally, the TGA profile for $CuWO_4$ (Na) displayed a mass loss region signaling decomposition of the material. As a result, the data shown for $CuWO_4$ (Na) and $CuWO_4$ (NH_4) are for the samples annealed at 400°C.

The Ag_2WO_4 (Na) XRD pattern suggests that the as-formed sample is already crystalline, thus requiring no further thermal annealing. Rietveld refinement confirmed a pure single phase orthorhombic crystal structure (space group *Pn2n*) in accordance with the JCPDS file and DFT calculations with a χ^2 value of 1.86. Multiple phases were present for the Ag_2WO_4 (NH_4) samples. The majority phase was found to be Ag_2WO_4 with a χ^2 value of 1.9 for the entire structure. All the Rietveld refinement analyses for the as-synthesized and highest annealed sample are shown in Figure 4-6.

The presence of additional peaks in the XRD pattern for the ammonium-derived samples may be a result of the use of a low pH from the addition of HNO_3. Recent literature supports this notion;[89,142] in the synthesis of $ZnWO_4$ via the hydrothermal process, WO_3 formation was noted in the XRD pattern when the solution mixture was at a low pH range (pH < 4). Additionally, the more exothermic environment (and consequently a faster reaction) in the case of the ammonium precursor can be another rationale for the appearance of the minority WO_3 phase.

The average crystallite sizes were calculated for the synthesized samples using the most intense peaks via the Scherrer equation. The first obvious trend is that the synthesized particles are nanocrystalline in nature, and the results show an increase in crystallite size with an increase in anneal temperature, as expected (see Table 4-1). Interestingly, the calculated crystallite size for the as-synthesized $ZnWO_4$ (Na) sample was as low as 1 nm. After annealing, all the tungstate samples synthesized with the ammonium precursor showed a smaller particle size compared to their counterparts using sodium-containing precursor. The smaller particle size appears to be associated with less single-phase material, as a result of the higher reaction temperature, and the greater amount of gas released during the synthesis. Note, however, that the Scherrer equation can only be applied to well-crystallized samples; otherwise XRD peak

broadening can reflect low crystallinity instead of nanosized entities; therefore the obtained crystallite sizes are considered as only estimates in these cases.

Table 4-1 Calculated average crystallite sizes of the various tungstate samples as a function of annealing and tungstate precursor.

SCS Sample		Crystallite size (nm)	
		As-synthesized	Annealed
$ZnWO_4$ (Na)		1 ± 7	32 ± 1
$CuWO_4$ (Na)		16 ± 1	22 ± 1
Ag_2WO_4 (Na)		22 ± 1	33 ± 2
$ZnWO_4$ (NH_4)	$ZnWO_4$	19 ± 1	23 ± 1
	WO_{3-x}	10 ± 1	16 ± 2
$CuWO_4$ (NH_4)	$CuWO_4$	21 ± 1	20 ± 1
	WO_{3-x}	11 ± 2	21 ± 10
Ag_2WO_4 (NH_4)	Ag_2WO_4	2 ± 6	14 ± 11
	WO_{3-x}	8 ± 2	15 ± 3

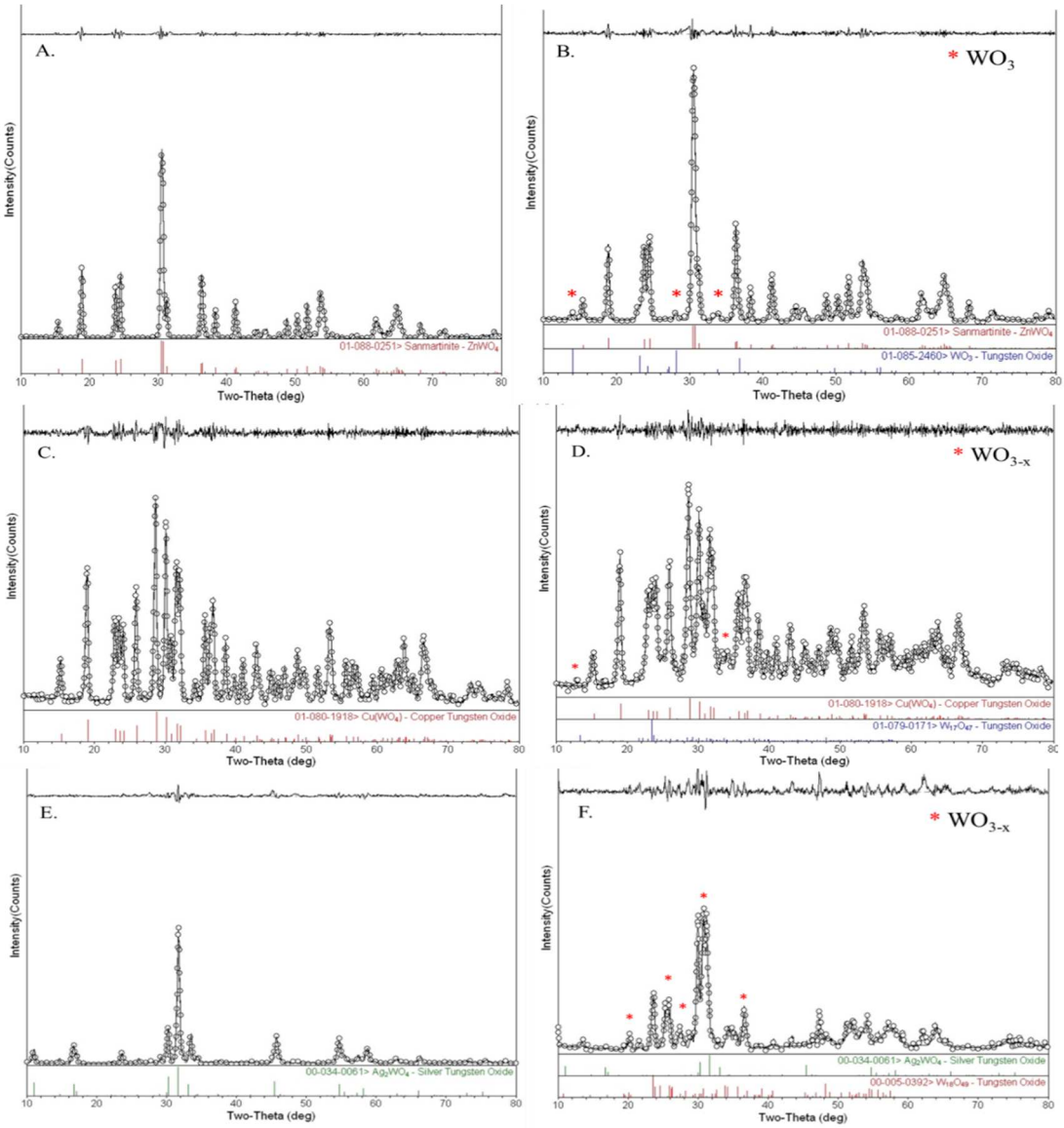

Figure 4-6 Rietveld refinement of A – B $ZnWO_4$ (Na) and $ZnWO_4$ (NH_4) respectively; C – D $CuWO_4$ (Na) and $CuWO_4$ (NH_4) respectively; and E – F Ag_2WO_4 (Na) and Ag_2WO_4 (NH_4) respectively.

TEM images of the SCS samples were additionally obtained so as to compare any contrasting morphologies that may arise due to the use of different precursors, see Figure 4-7. In general, the particle sizes obtained from TEM were larger than the calculated crystallite sizes from XRD data (or in other words the size of the crystalline domains). As for $CuWO_4$ (similarly for both precursors), the as-synthesized samples yielded particle sizes ranging from 15 – 50 nm with the size increasing with increasing anneal temperature. Figure 4-7 shows samples with rounded edges signaling that they are at least partly in an amorphous phase. Closer inspection, however, revealed crystalline domains, where the lattice fringes were visible (corresponding to the [011] lattice plane),[143] in agreement with the previously presented XRD data.

In contrast, the as-synthesized $ZnWO_4$ (Na) was completely amorphous with agglomerated small-sized nanoparticles. For the annealed $ZnWO_4$ samples, however, sharp edges of much larger particles were seen, indicating improved crystallinity consistent with the XRD patterns. The most interesting morphological feature was noted for the $ZnWO_4$ (NH_4) samples (Figure 4-7), where the sample showed partial crystallinity, and well-defined hexagonal nanorod morphology even *without* heat treatment, again corroborating the previously shown XRD patterns. Note that this kind of morphology was observed for $ZnWO_4$ before, although as a result of a lengthy hydrothermal synthetic procedure.[87,142,144] HR-TEM images confirmed that $ZnWO_4$ nanorods preferentially grew along the [100] direction. Interplanar spacings were determined to be 0.575 nm and 0.468 nm corresponding to the [101] and [100] lattice planes, respectively, consistent with earlier reports.[142,145] Besides the rod-shaped crystals, some spherical-shaped nanoparticles can be also seen in the images for the as-synthesized samples, while strictly rod-shaped crystals (lengths 100 – 150 nm) are present after annealing.

Ag_2WO_4 (Na) appeared to form much smaller particles compared to the other cases with sizes in the 4 – 10 nm range with many of the particles covered by a thin carbon film (as residue from the SCS precursor). Notably, such carbon coating can be indeed useful for certain applications, such as in Li-ion batteries, an alternative application area of these binary tungstates.[145,146] Upon subsequent heat treatment, this carbon matrix is removed, and large aggregates of the small nanoparticles can be observed. Overall, we can conclude that a variety of morphologies can be achieved upon using different precursors, and subsequent heat treatment, tailoring the morphology of these oxides towards a targeted application.

Further structural analysis of the synthesized tungstates was performed using Raman spectroscopy (Figure 4-9). Using group theory, different studies have reported the existence of as many as 18 Raman-active vibrational modes for $ZnWO_4$ and $CuWO_4$.[147-149] Experimental results show 10 – 11 of the Raman active vibrations for both oxides within the frequency range of the experiment. Of the 10 Raman-active bands observed, 5 - 6 internal stretching modes were present due to the W – O bonds in the WO_6 octahedra of the metal tungstate structure. Importantly, assignment of the Raman bands (see Table 4-2 – 4-4) confirmed the formation of the respective compound structures for all the samples. The positions of the most intensive band in each sample corresponding to the W – O stretching mode were 907 cm^{-1}, 899 cm^{-1}, and 883 cm^{-1} for $ZnWO_4$, $CuWO_4$, and Ag_2WO_4 respectively. The 805 cm^{-1} vibrational mode characteristic of WO_3 appeared in all the samples prepared with ammonium tungstate, thus confirming the multiphase structure.[150]

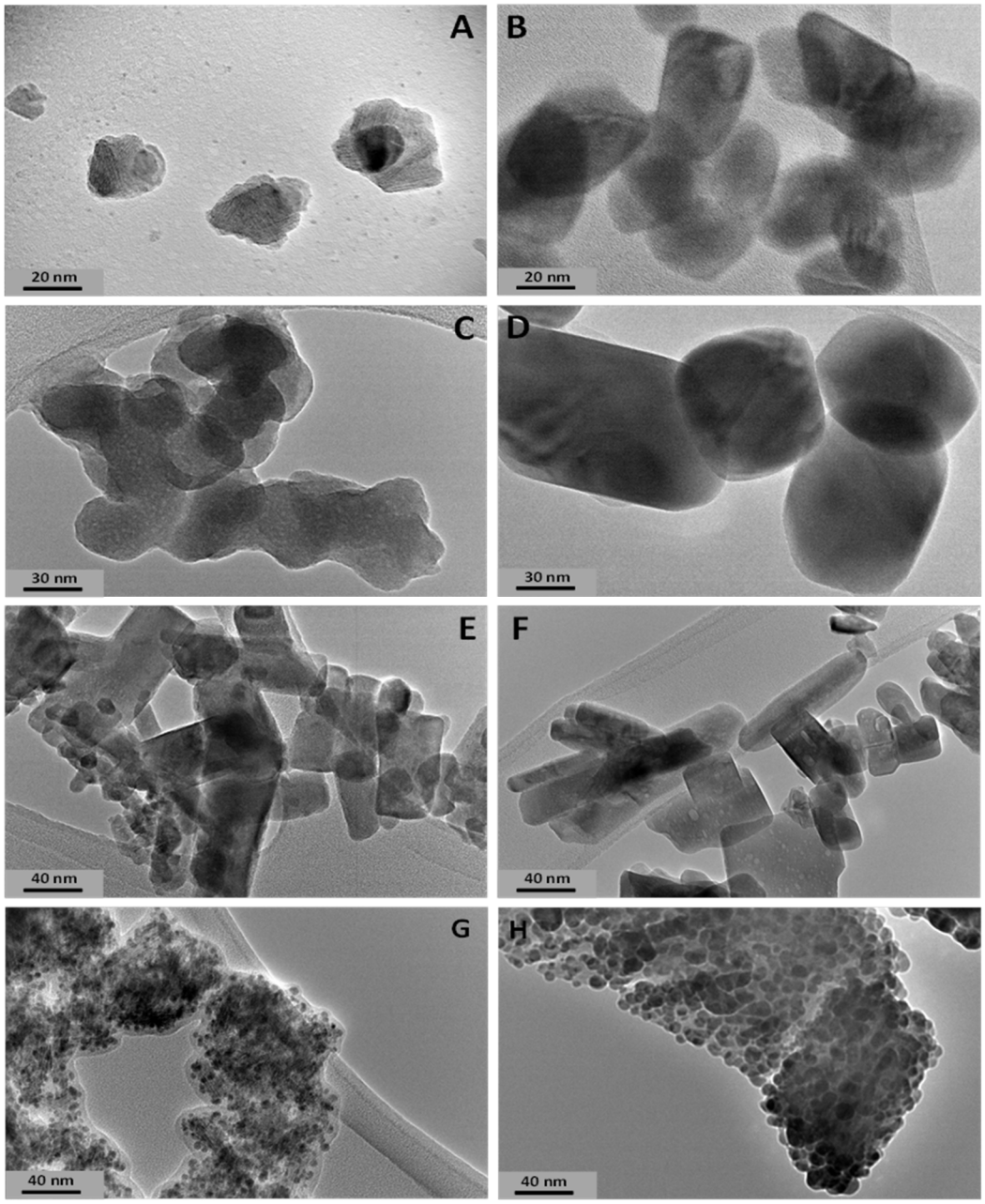

Figure 4-7 TEM images of A-B $CuWO_4$ (Na) as-synthesized and annealed at 400°C respectively; C-D $ZnWO_4$ (Na) as-synthesized and annealed at 500°C respectively; E-F $ZnWO_4$ (NH_4) as-synthesized and annealed at 500°C respectively; G-H Ag_2WO_4 (NH_4) as-synthesized and annealed at 500°C.

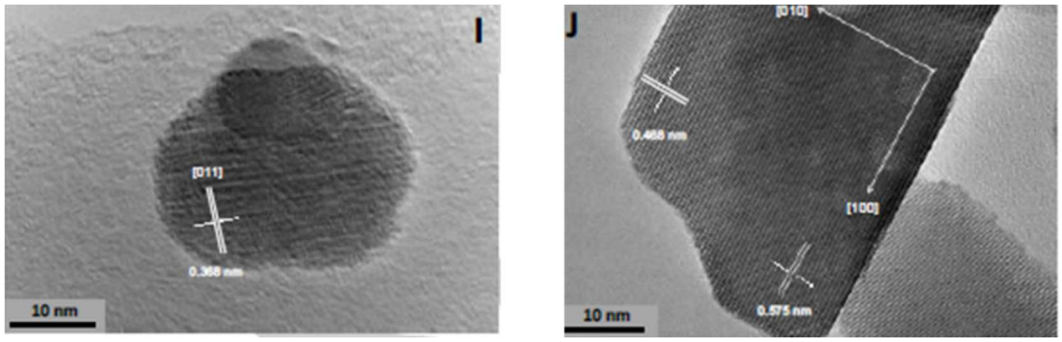

Figure 4-8 I and J are HR-TEM images of the nanoparticles in Figure 4-7 A and E.

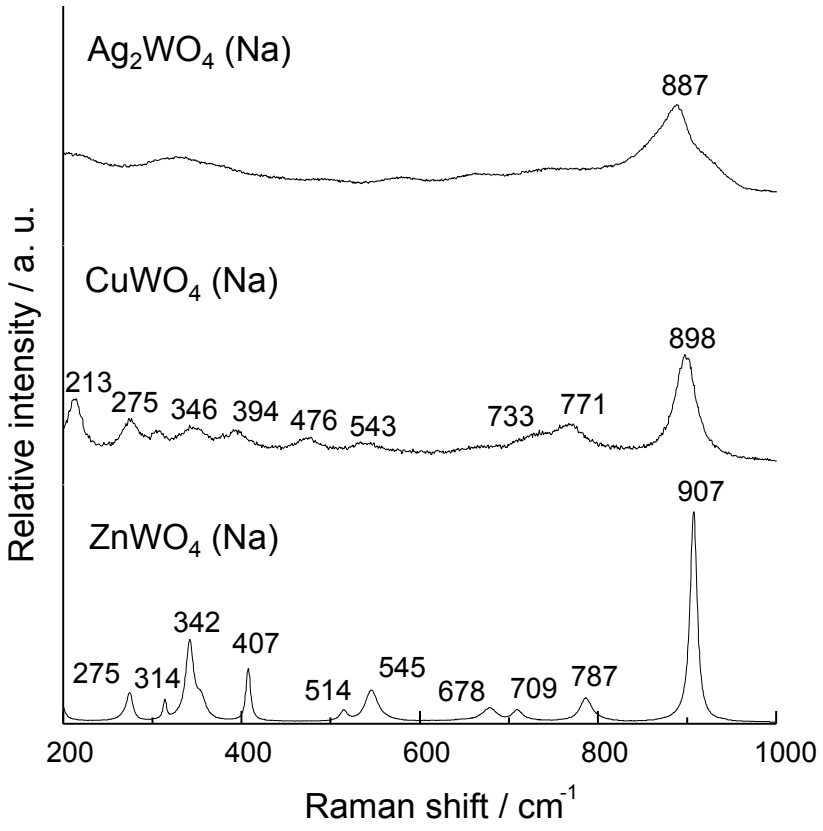

Figure 4-9 Raman spectra of $ZnWO_4$ (Na), $CuWO_4$ (Na), and Ag_2WO_4 (Na) samples.

Table 4-2 Raman vibrations of SCS $ZnWO_4$.

Raman Mode	Raman signals (cm^{-1})		Reported Values [145,147-149] (cm^{-1})
	$ZnWO_4$ (Na)	$ZnWO_4$ (NH_4)	
A_g [a]	907	909	906,906,906
E_g	-	805	-
B_g [a]	787	784	785,785,782
A_g [a]	709	708	708,708,707
B_g [a]	678	678	677,680,676
A_g [a]	545	545	545,544,541
B_g	514	515	514,515,510
A_g [a]	407	406	407,408,404
B_g	-	-	355
A_g	342	341	343,342,336
B_g	314	315	314,314,311
A_g	275	277	275,275,270

[a] = Internal stretching modes

Table 4-3 Raman vibrations of SCS $CuWO_4$.

Raman Mode	Raman signals (cm^{-1})		Reported Values [91,151] (cm^{-1})
	$CuWO_4$ (Na)	$CuWO_4$ (NH_4)	
A_g [a]	899	898	906,905
E_g	-	808	805
B_g [a]	771	774	779,778
A_g [a]	733	731	733,731
B_g [a]	673	675	676,673
A_g [a]	543	536	550,547
B_g	476	475	479,477
A_g [a]	-	-	405
A_g	394	393	398,395
B_g	346	348	358,355
A_g	305	304	315,314
B_g	275	274	293,279
A_g	213	211	283,223

[a] = Internal stretching modes

Table 4-4 Raman vibrations of SCS Ag_2WO_4.

Raman Mode	Raman signals (cm^{-1})		Reported Values[88] (cm^{-1})
	Ag_2WO_4 (Na)	Ag_2WO_4 (NH_4)	
A_g [a]	883	896	878
E_g	-	808	-
A_g [a]	-	-	799
A_g	-	-	774
B_g [a]	-	752	757
B_g	-	673	661
A_g	-	-	578
B_g [a]	-	-	504
B_g [a]	-	-	485
A_g [a]	-	384	363
B_g [a]	-	-	332
A_g [a]	301	296	302
B_g	-	246	246
A_g	-	211	204

[a] = Internal stretching modes

4.1.3. Optical Properties and Electronic Band Structure

UV-vis diffuse reflectance spectroscopy was utilized to estimate the band gap values of the synthesized oxides. Tauc plots were generated for all the SCS samples and are illustrated below in Figures 4-10 – 4-12. Experimental optical measurements for $ZnWO_4$ yielded direct bandgap values ranging from 3.24-3.89 eV (indicative of UV light absorption) all within range of previous synthesis studies. $CuWO_4$ and Ag_2WO_4 samples showed indirect bandgap values ranging from 1.80-2.04 eV and 2.44-3.10 eV respectively; both correspond to previously reported literature values (see Table 4-3). The resulting tungstate products described above were observed to be white, yellow-brown, and gray in color for $ZnWO_4$, $CuWO_4$, and Ag_2WO_4 respectively (see Figure 4-13).

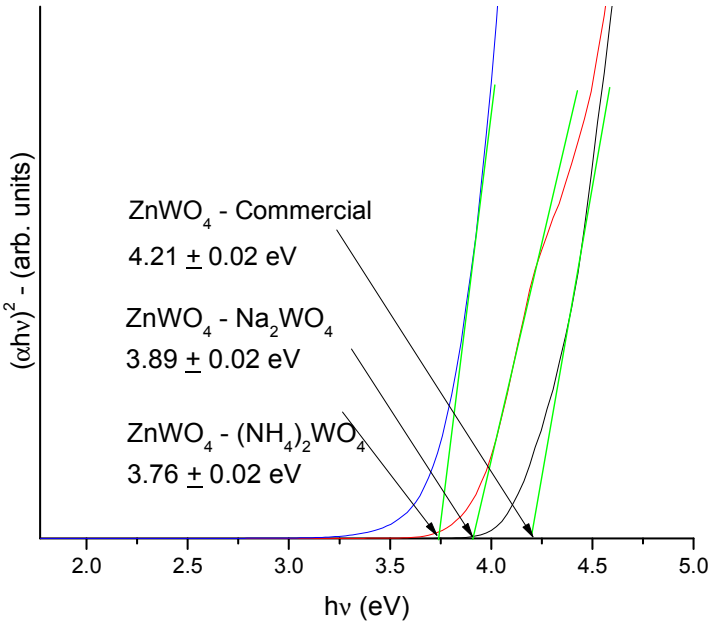

Figure 4-10 Tauc plots showing band gap values for $ZnWO_4$ samples.

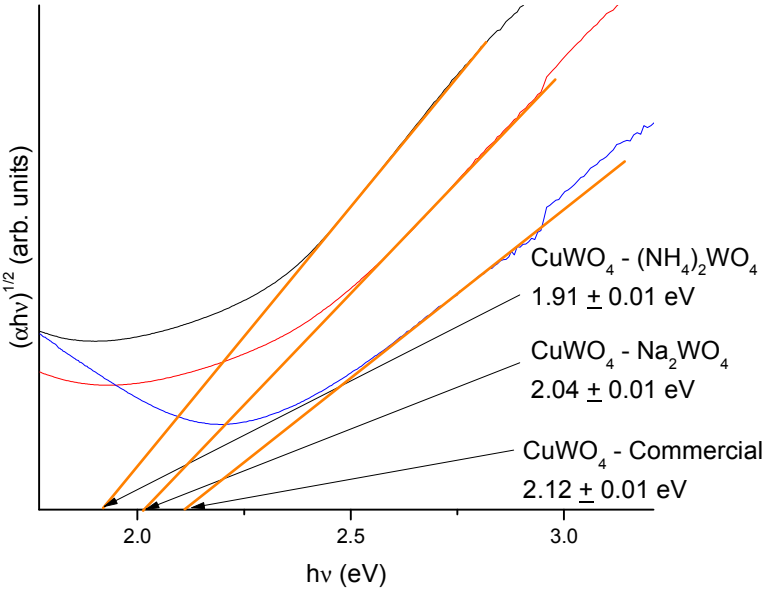

Figure 4-11 Tauc plots showing band gap values for $CuWO_4$ samples.

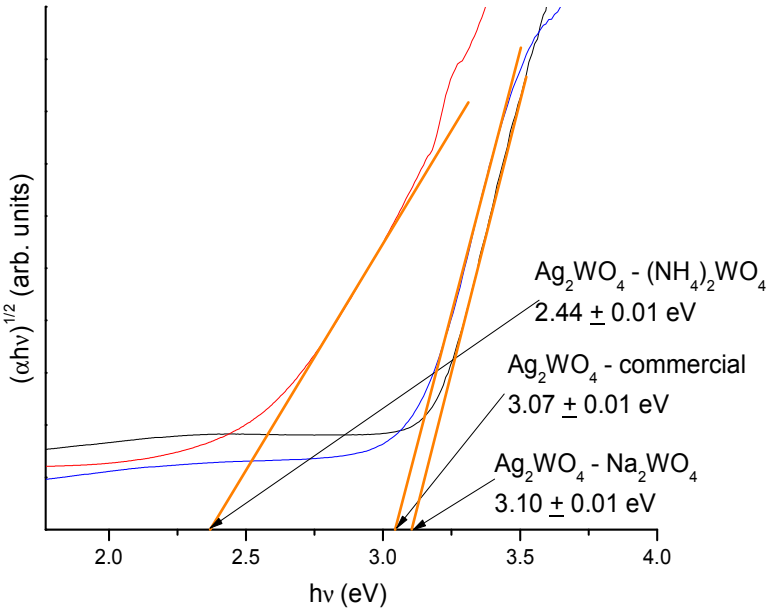

Figure 4-12 Tauc plots showing band gap values for Ag_2WO_4 samples.

Table 4-5 Optical properties of the synthesized samples using different tungsten precursors.

Sample	Direct Band Gap (eV)		Calculated band gap values (eV)	Reported values (eV)
	As-synthesized	Annealed at highest temperature		
$ZnWO_4$ (Na)	3.89 ± 0.02	3.24± 0.03	2.92	3.02 – 5.85[86,87,93]
$ZnWO_4$ (NH_4)	3.76 ± 0.02	3.45± 0.03		
	Indirect Band Gap (eV)			
	As-synthesized	Annealed at highest temperature		
$CuWO_4$ (Na)	2.04 ± 0.01	2.03± 0.01	2.10	1.78 – 2.79[78,91-93]
$CuWO_4$ (NH_4)	1.91± 0.01	1.80± 0.01		
Ag_2WO_4 (Na)	3.10 ± 0.01	-	1.22	3.06 – 3.55[81,83,88]
Ag_2WO_4 (NH_4)	2.44 ± 0.01	2.83± 0.02		

Figure 4-13 Photographs of the SCS tungstate samples using Na_2WO_4.

Computational studies (Dr. Huda's group) were performed to rationalize the above optical properties, and to correlate them with the photocatalytic activity of these materials (discussed below). The electronic band structure for each of the tungstate materials were calculated along the special symmetry points in the Brillouin zone. The DFT + U electronic band gap structure for $ZnWO_4$ presents a direct band gap of 2.94 eV (very close to the calculated optical absorption) occurring at the Z point. In Figure 4-14, the VB is dispersive throughout all the regions indicating lower effective masses of holes. Similar dispersive features are also found for the CB along the regions except D to B which suggests higher effective masses of electrons, while other regions indicate lower effective masses of electrons. In addition, the presence of these lower effective masses of electron regions suggests an ease of transfer of electrons from the VB to the CB. The calculated optical band gap (2.92 eV) corresponds to the electronic band gap. Since the d-d electron transition is forbidden and the top of VB is largely contributed by O 2p, the first peak at 3.43 eV corresponds to electron transfer from O 2p at the top of VB to W 5d at the bottom of CB at the Z point.

In Figure 4-15, an indirect band gap with a minimal value of 0.707 eV occurs along the Y→Γ region for $CuWO_4$. The VB along the Γ→X regions is very flat suggesting

higher effective mass of holes. The CB is divided into two regions in which the first region contains only two bands which are mid-gap levels at 0.707 eV higher than the VB and dispersive throughout all symmetry points. The bottom of the CB of the second region is about 3.087 eV higher from the VB maximum. They are flat along Γ→X and R→T, however, dispersive along the other symmetry points. The minimal optical band gap was calculated to be 2.1 eV. By comparing optical absorption and band structure, it can be concluded that electron transition does not occur between the top or just below the top of the VB and bottom or just above the bottom of the CB which are dominated by Cu 3d and W 5d, respectively since the d-d transition is forbidden. Hence, the origin of the optical gap is attributed to electron transfer from occupied O 2p states within the VB to the unoccupied Cu 3d mid-bands (first part of CB).

For Ag_2WO_4, an indirect band gap value of 1.17 eV was found between X and Γ (Figure 4-16). Along the Y-S-X region, the mid-gap bands are degenerate. Moreover, the less dispersive nature of the bands in both VB and CB along this region suggests higher effective masses and hence, lowers conductivity for both electrons and holes. The computed band gap corresponds to optical transition due to electron transfer from O 2p at the top of the VB to W 5d/Ag 4d at the bottom of the mid-gap CB, or, from Ag 4d at the top of the VB to O 2p at the bottom of the mid CB. Both these values are smaller than the experimentally measured band gaps for as-synthesized Ag_2WO_4 (Na) and Ag_2WO_4 (NH_4) samples.

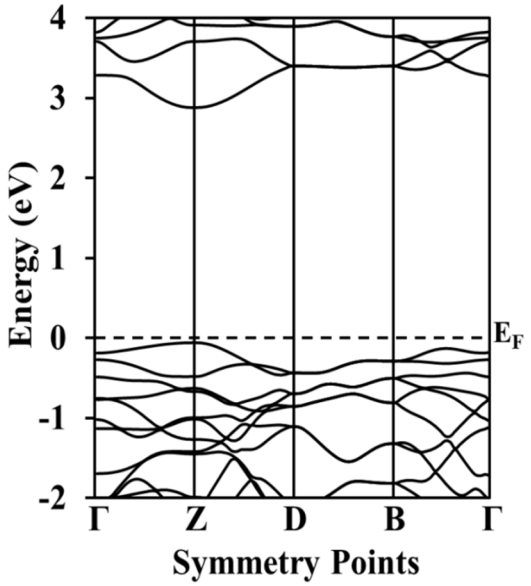

Figure 4-14 Electronic band structure for $ZnWO_4$.

(Courtesy Dr.Muhammad Huda's group – Physics Department)

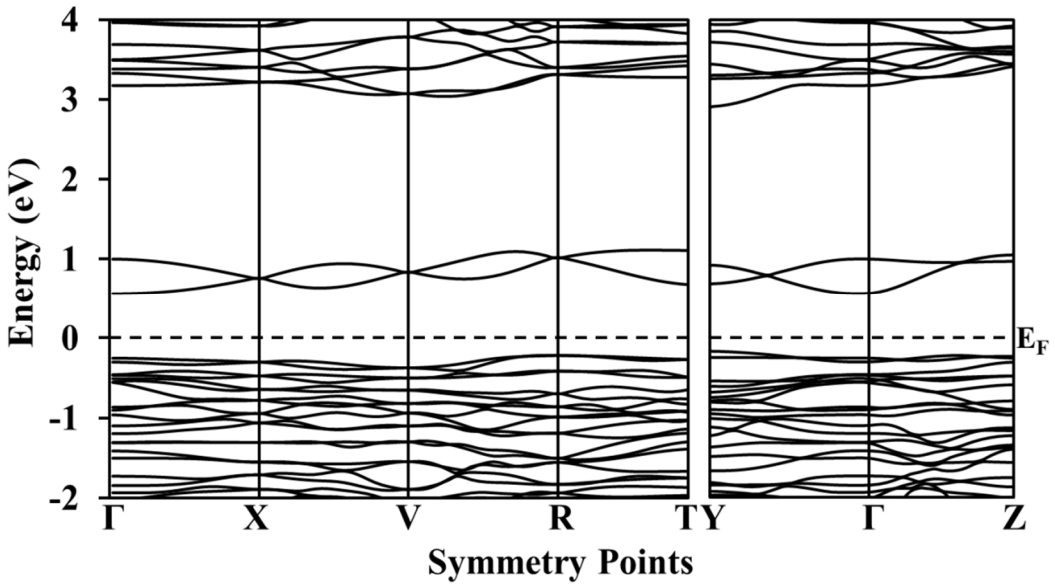

Figure 4-15 Electronic band structure for $CuWO_4$.

(Courtesy Dr. Muhammad Huda's group – Physics Department)

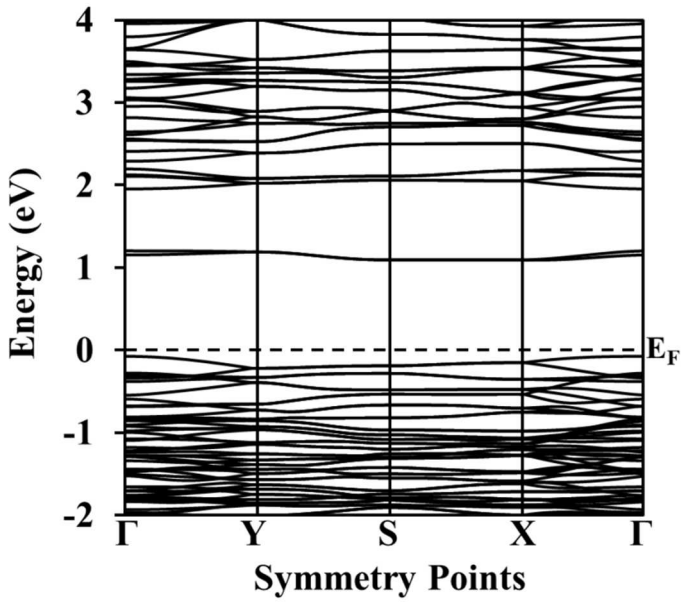

Figure 4-16 Electronic band structure for Ag_2WO_4.

(Courtesy Dr. Muhammad Huda's group – Physics Department)

4.1.4. Photocatalytic Behavior

Figures 4-17 – 4-19 compare the photocatalytic activity profiles for MO dye degradation for the blank case (no photocatalyst present), the commercial sample, and the newly synthesized nanoparticles. Clearly, the newly synthesized nanoparticles showed good photocatalytic activity compared to the commercial samples under UV irradiation. In fact, $ZnWO_4$ (Na) exhibited the best photocatalytic activity compared to $ZnWO_4$ (NH_4) and the commercial samples, most likely due to its pure, monoclinic single phase structure and relatively small particle size. At 20 – 40 min of irradiation both $ZnWO_4$ (Na) and $ZnWO_4$ (NH_4) had degraded the MO dye ~90%, while the commercial sample took much longer. Additionally, results show that both samples of $CuWO_4$ and

Ag_2WO_4 out-performed their respective commercial counterparts, with a striking difference for the $CuWO_4$ samples.

Aside from UV-Visible spectrophotometry, LC-MS was also used to monitor the photocatalytic degradation of methyl orange. As represented by $ZnWO_4$ (Na) in Figure 4-20, there is a definite decrease in the ion peak area for methyl orange (m/z = 304.07 in negative ion mode) with reaction time. More importantly, the degradation pattern is similar to that derived from UV-visible spectrophotometry: the methyl orange concentration reached zero within 40 min. Using MS^2, major intermediates were detected and similar oxidative degradation pathways were identified to that of previously reported experiments with TiO_2, involving demethylation and hydroxylation intermediate steps.[152,153]

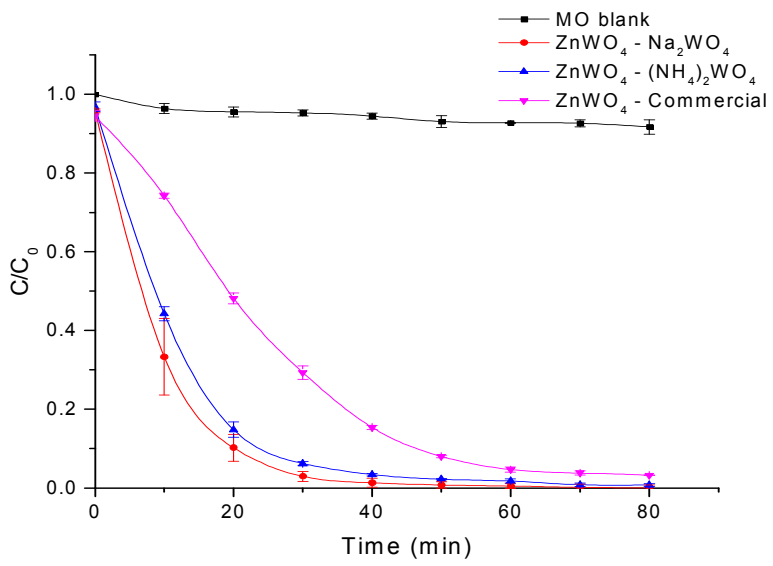

Figure 4-17 Methyl orange photodegradation using the as-synthesized $ZnWO_4$ samples under UV – Visible light irradiation.

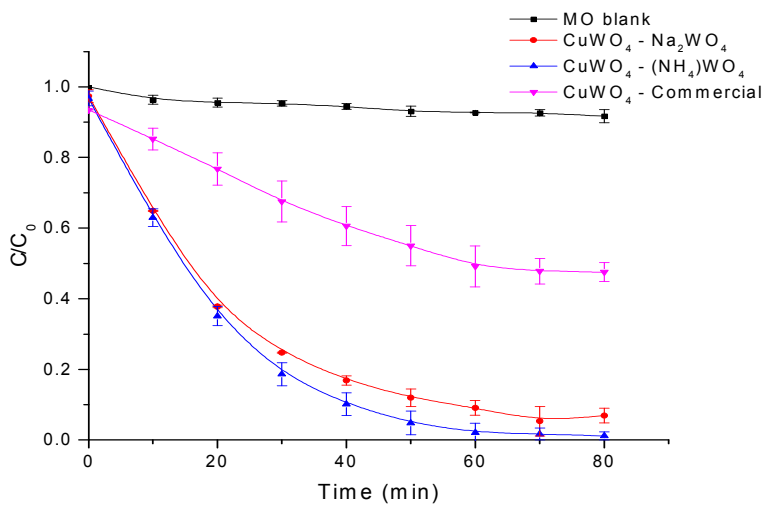

Figure 4-18 Methyl orange photodegradation using the as-synthesized $CuWO_4$ samples under UV – Visible light irradiation.

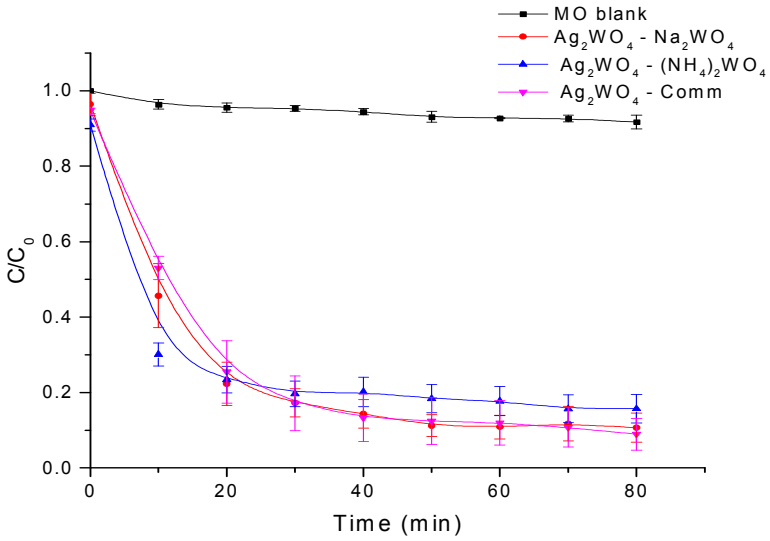

Figure 4-19 Methyl orange photodegradation using the as-synthesized Ag_2WO_4 samples under UV – Visible light irradiation.

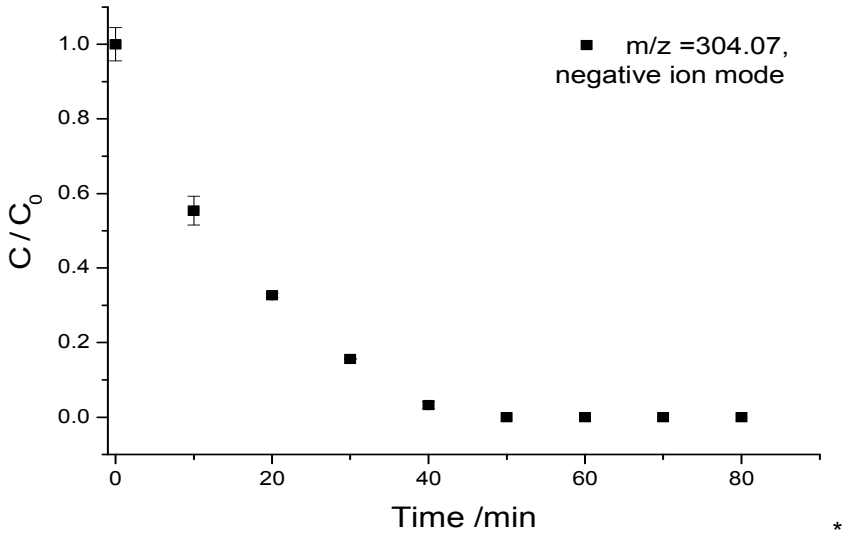

Figure 4-20 LC-MS monitoring of methyl orange degradation using $ZnWO_4$ (Na) under UV-visible light irradiation.

Linear regression was performed for the first 40 min of each photodegradation profile data see Table 4-4. The apparent rate constants shown in Figure 4-21 suggest that the solution combustion synthesized samples exhibited faster kinetics for MO dye degradation than their respective commercial samples, with the k_{app} trending thus: $ZnWO_4$ > $CuWO_4$ ~ Ag_2WO_4. The enhanced degradation rate of these nanoparticles especially $ZnWO_4$ perhaps can be attributed to more optimal optical, electronic, structure/morphology, and surface properties.

Table 4-6 Apparent rate constants for MO photodegradation.

Photocatalyst	k_{app} x 10^{-2} (min^{-1})	R^2
$ZnWO_4$ (Na)	11.0	0.994
$ZnWO_4$ (NH_4)	8.6	0.988
$ZnWO_4$ Commercial	4.5	0.965
$CuWO_4$ (Na)	4.4	0.995
$CuWO_4$ (NH_4)	5.7	0.993
$CuWO_4$ Commercial	2.6	0.979
Ag_2WO_4 (Na)	4.5	0.997
Ag_2WO_4 (NH_4)	3.3	0.894
Ag_2WO_4 Commercial	2.4	0.991

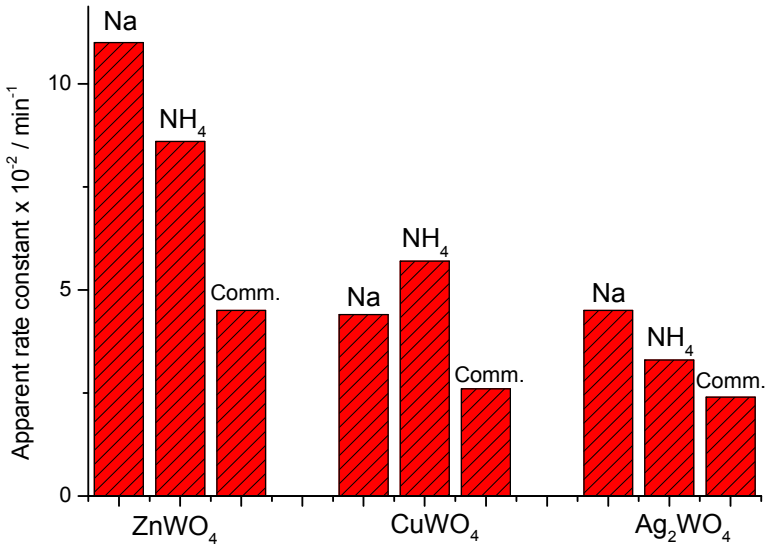

Figure 4-21 Comparison of the linear regression apparent rate constant values from methyl orange photodegradation.

For a given photocatalytic material, surface area (BET surface area data listed in Table 4-7) and surface chemical properties can dictate the amount of substrate species that are initially bound via adsorption. As a result, the kinetics of each material adsorption was studied with an equilibrium reached approximately within 40 – 50 min (see Figure 4-22). For this reason, a 60 min incubation period was used for the photocatalysis process. The amount of adsorbed dye was determined for all the samples (see Figure 4-23); most values of the adsorbed dye amount fall within the same range of 15 – 25 μmolg^{-1}, except for the commercial $CuWO_4$ and Ag_2WO_4 (NH_4) which had higher values (~65 μmolg^{-1}). Most importantly, the rate limiting step for this experiment was not dye adsorption. If that

were the case, the commercial $CuWO_4$ and Ag_2WO_4 (NH_4) should have outperformed their counterparts because of the larger adsorbed dye amounts. In fact, the commercial $CuWO_4$ showed the worst photocatalytic activity of all the studies. Such observations suggest that factors other than surface area and dye adsorption play a role in the increased photocatalytic activity of the SCS tungstate nanoparticles.

Table 4-7 BET surface area values for the SCS tungstate samples and commercial benchmarks.

Material	S_{BET} (m^2/g)
$ZnWO_4$ (Na)	11.93
$ZnWO_4$ (NH_4)	11.78
$ZnWO_4$ Commercial	45.84
$CuWO_4$ (Na)	14.35
$CuWO_4$ (NH_4)	13.23
$CuWO_4$ Commercial	42.27
Ag_2WO_4 (Na)	21.34
Ag_2WO_4 (NH_4)	51.55
Ag_2WO_4 Commercial	19.35

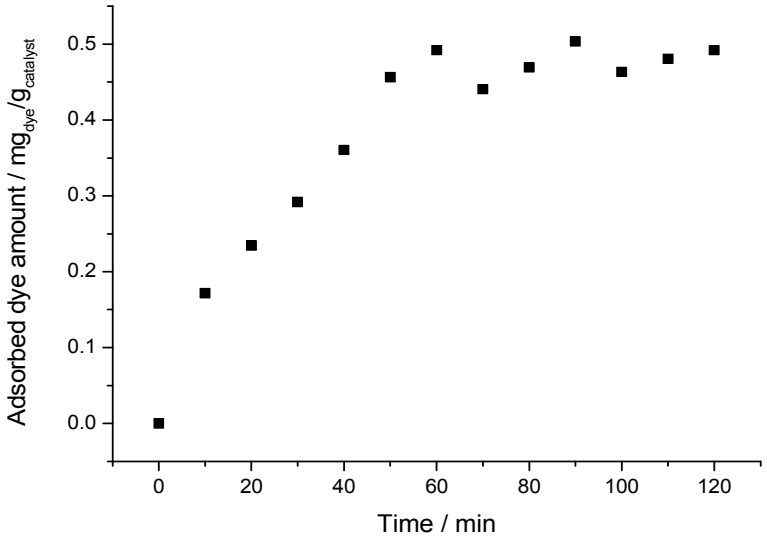

Figure 4-22 Adsorption kinetics of methyl orange on $ZnWO_4$ (NH_4, as-is) with a 2 g/L catalyst concentration and 50 µM methyl orange solution concentration.

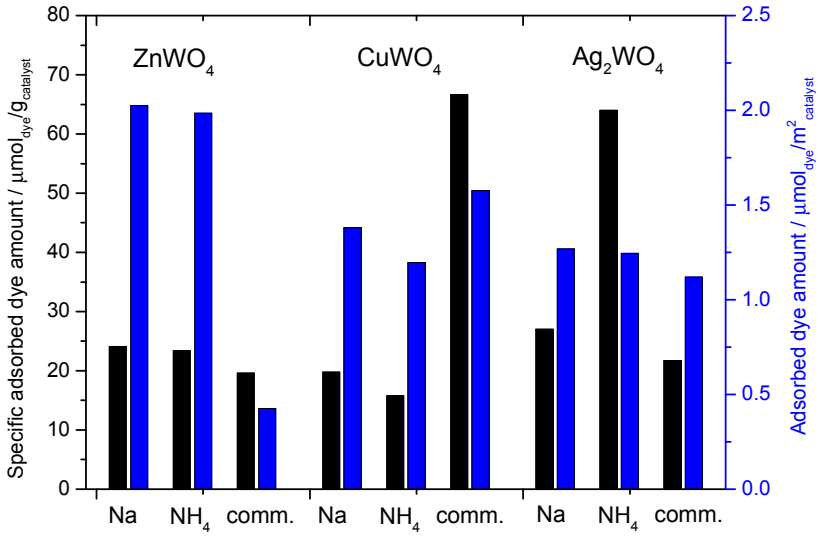

Figure 4-23 Comparison of the specific-, and surface area normalized amounts of adsorbed methyl orange for the different tungstate samples. The catalyst concentration was 2 g/L, while the concentration of the methyl orange solution was 200 µM.

The crystallinity of a material is of great importance in improving/enhancing the photocatalytic performance. However in our case, this statement can be misleading in that varying levels of crystallinity exist for these newly synthesized tungstate materials. For example, $ZnWO_4$ (Na) and $ZnWO_4$ (NH_4) show similar performances, although they display very different crystallinities (see Figure 4-3). Along with crystallinity, phase purity can also have a significant impact on performance. As a matter of fact, it may well be the reasoning behind the poor performance of the commercial tungstate samples.

4.1.5. Photoelectrochemical Behavior

Based on electronic properties, the valence band edge positions of tungstate materials can lead to variations in oxidative photocatalytic activities. That being the case, linear sweep photovoltammograms were recorded for the SCS samples. Surprisingly, the highest photocurrents came from $CuWO_4$ (Figure 4-24 A). Stable, but low photocurrents were observed for $ZnWO_4$, while under those conditions, Ag_2WO_4 was unstable. Photovoltammograms, employing a narrower potential window spanning the open-circuit potential under illumination (Figure 4-24 B), were also recorded in sulfite (hole scavenger) ion containing electrolyte. The onset potential of these curves can be associated with the Fermi level of the various semiconductor samples, and thus their relative position can be correlated to the position of the CB edge.[154]

Therefore, considering the obtained band gap energies and potential increase for Zn, Ag, and Cu-series of -0.2 V, -0.1 V, and +0.05 V respectively (see arrows in Figure 4-24B), the high photocatalytic activity of $ZnWO_4$ can be attributed to its more positive VB edge position. This can result in higher oxidation power of the photogenerated holes. Although $CuWO_4$ yielded a high photocurrent, its less positive VB edge position lead to much lower photocatalytic activity.

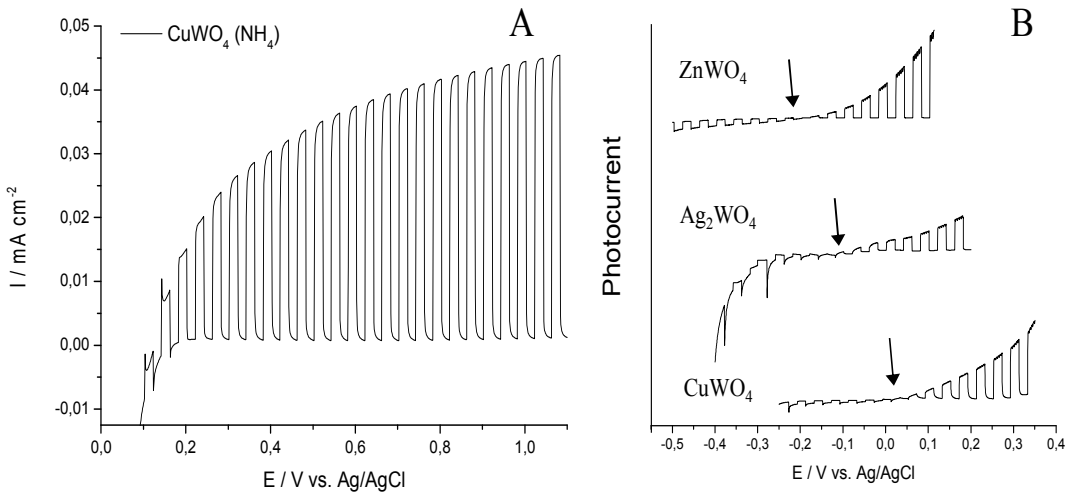

Figure 4-24 A. Photovoltammogram of a $CuWO_4$ (NH_4) sample recorded between 0.1 V and 1.1 V, in 0.1 M Na_2SO_4, at a sweep rate of 2 mV s^{-1} using a 300W Hg-Xe arc lamp. B. Comparison of the onset potential for the three tungstate samples in 0.1 M Na_2SO_3.

4.2. Niobium-based Oxide Semiconductors

4.2.1. Thermal Analysis

A better understanding of the decomposition of the precursor mixture within the SCS process can be provided by doing thermal analysis. For that reason, thermogravimetric analysis/differential scanning calorimetry (TGA/DSC) was employed to simulate the SCS reaction process. The TGA/DSC profiles for both material precursor mixtures are displayed below in Figure 4-25.

The precursor mixtures utilized for each simulated reaction show the presence of multiple mass loss regimes as observed in the corresponding TGA profiles (Figure 4-25 A). The first mass loss occurs between 100 – 150˚C, assignable to the elimination of

water in both cases. Thereafter, for the copper niobate precursors, the mass loss above 200˚C was observed as a single step. This can be attributed to the onset of combustion reaction and the subsequent combined decomposition of the metal salt precursor and fuel. The zinc niobate precursor mixture, however, had an expanded temperature range of 140 – 410˚C corresponding to the decomposition of the metal salt precursor and the fuel.

Both endothermic and exothermic peaks were observed in the DSC analysis profiles as shown in Figure 4-25 B. Fairly broad endothermic peaks were seen at the initial stage of analysis, assignable to the first water loss within each precursor mixture; these correspond to the first mass loss regime in the TGA profile. Evidence for a more combustible reaction for the copper niobate precursor can be seen in the sharp exothermic peak present with similar results reported in the thermal decomposition of freeze-dried complex oxalate solutions.[104] Additionally, these sharper exothermic peaks suggest a more combustible reaction compared to the zinc niobate precursor. Two exothermic peaks were witnessed at approximately 250˚C and 560˚C coinciding with the initiation of the combustion reaction accompanied by oxidative decomposition of the fuel, as well as crystallization of the product material.

4.2.2. Structural and Morphological Determination

The crystalline phase of the as-synthesized, annealed, and respective commercial samples were characterized using powder X-ray diffraction (XRD), along with Rietveld refinement analysis. Each of the combustion synthesized samples were annealed at 600°C in order to enhance the degree of crystallinity, as well as to remove any impurity or carbon residue that may be present. It can be noted that even without additional heat treatment, fairly crystalline products was observed for both SCS samples. Figures 4-26 A and B illustrate the XRD patterns of $ZnNb_2O_6$ and $CuNb_2O_6$ respectively.

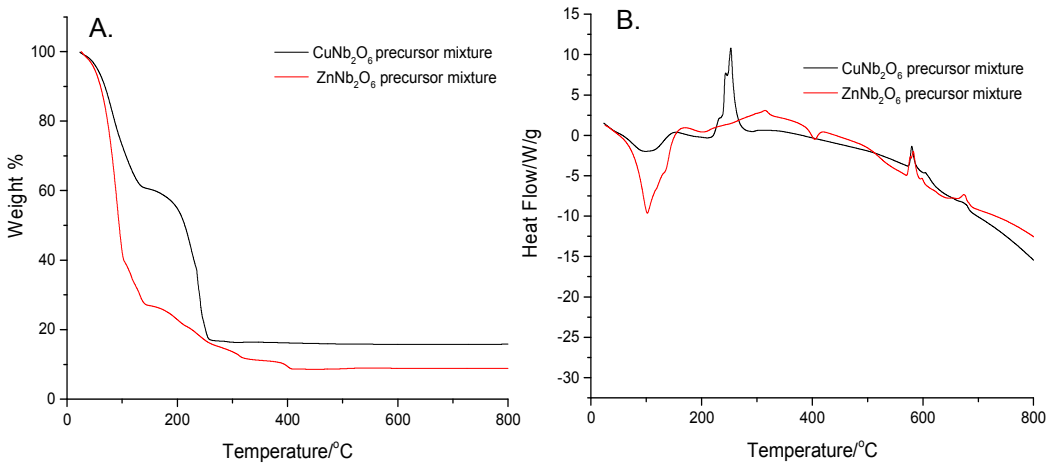

Figure 4-25 A. TGA and B. DSC profiles of the copper and zinc niobate precursor mixtures.

Detailed Rietveld refinement of the annealed $ZnNb_2O_6$ sample yielded a multiphase structure comprising of an orthorhombic $ZnNb_2O_6$ (majority) and ZnO (minority) phase, both matching with their JCPDS files 76-1827 and 89-0511 respectively. ZnO perhaps was generated from decomposition of zinc nitrate before being calcined by the internal temperature and subsequent annealing. The commercial sample, however, was of a single phase structure exhibiting high crystallinity as illustrated in Figure 4-26 A.

The $CuNb_2O_6$ XRD pattern before and after heat treatment clearly yielded a material more crystalline in nature; this is in accordance with the reaction's exothermicity. Rietveld analysis of the annealed sample gave rise to a single phase monoclinic $CuNb_2O_6$ structure (see Figure 4-26 B) in agreement with the 83-0369 JCPDS file. An earlier report has shown that $CuNb_2O_6$ favors the monoclinic structure if oxalate precursor is used in the preparation.[104] Although good crystallinity was exhibited by the

commercial $CuNb_2O_6$ sample, a multiphase structure was determined with the minute secondary phase being Nb_2O_5.

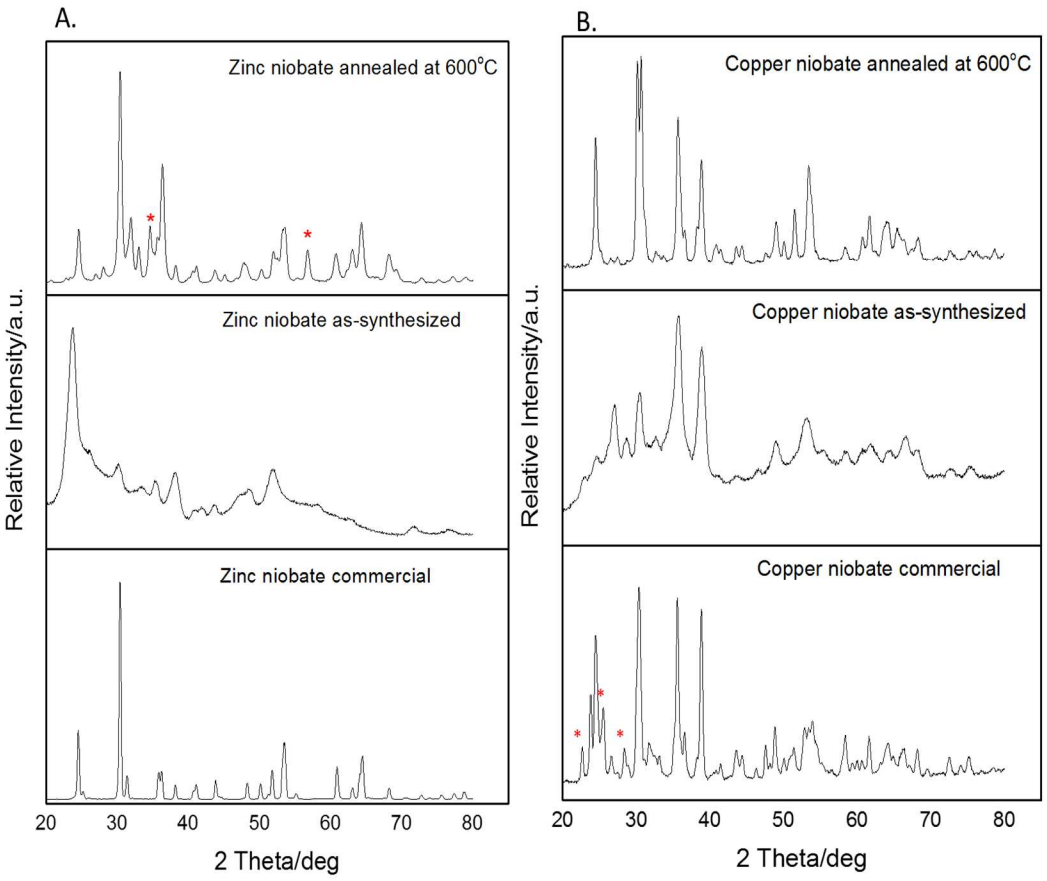

Figure 4-26 XRD patterns of A. $ZnNb_2O_6$ and B. $CuNb_2O_6$ samples; (*) represents the presence of ZnO in the sample and Nb_2O_5 in $ZnNb_2O_6$ and $CuNb_2O_6$ respectively.

The most intense XRD peaks were used to calculate the average crystallite sizes of each material. As displayed in Table 4-8 below, there is a clear and expected trend that the nano-sized particles increased with anneal temperature. In addition, the BET analysis results in turn showed a decrease in the BET surface area for each of the samples. This can be attributed to the increase in the particle size at the higher temperatures.

Table 4-8 Calculated average crystallite sizes and surface area values for the SCS niobate samples as a function of annealing temperature.

Semiconductor material		Crystallite size (nm)	Surface area (m^2/g)
$ZnNb_2O_6$	As-synthesized	4 ± 2	64.9
	Annealed at 600˚C	15 ± 3	18.4
	Commercial	31 ± 3	0.4
$CuNb_2O_6$	As-synthesized	8 ± 1	16.0
	Annealed at 600˚C	20 ± 2	8.8
	Commercial	19 ± 3	0.9

Further examination of the structural morphologies of the SCS samples was carried out by SEM and TEM imaging of each SCS sample. The particle sizes obtained

from both images were larger than the calculated crystallite sizes from the XRD pattern (or in other words the size of the crystalline domain). The as-synthesized samples showed severely agglomerated, irregularly shaped small sized particles with a mixture of round and sharp edges, signaling that they are partially crystalline in nature. With additional heat treatment, reduced agglomeration was observed yielding particles of larger sizes (Figure 4-27). For both $CuNb_2O_6$ and $ZnNb_2O_6$ as-synthesized samples, the particle size ranged from 15 nm to 30 nm. Closer inspection of the particles via HR-TEM (see Figure 4-28) revealed visible lattice fringes which correlate to the XRD pattern previously mentioned above. At the 600˚C anneal temperature, both SCS samples showed a decreased degree of agglomeration with larger particles observed ranging from 20 nm to 60 nm with improved crystallinity.

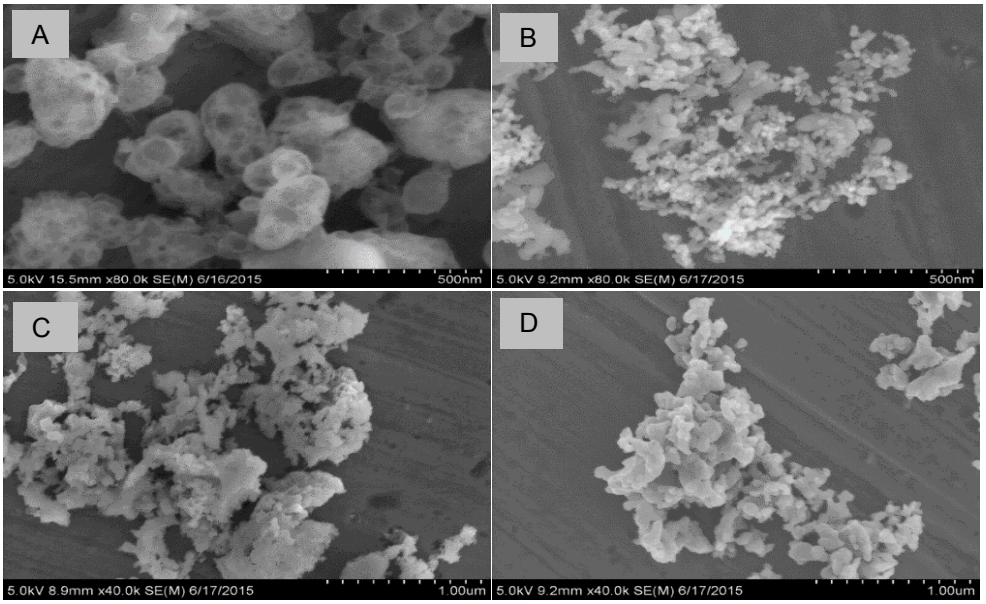

Figure 4-27 SEM images of A-B. $ZnNb_2O_6$ as-synthesized and annealed at 600°C respectively and C-D. $CuNb_2O_6$ as-synthesized and annealed at 600°C respectively.

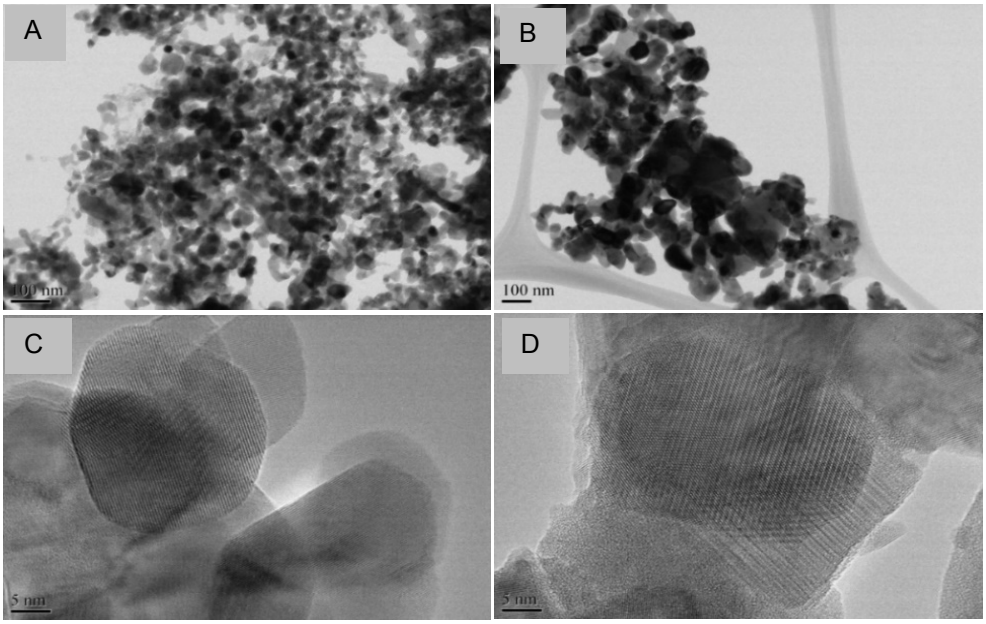

Figure 4-28 TEM images of A-B $ZnNb_2O_6$ and $CuNb_2O_6$ annealed at 600°C respectively and C-D HR-TEM images of images A, B respectively, displaying the presence of lattice fringes.

4.2.3. Optical Properties

UV-Visible diffuse reflectance spectroscopy was employed to estimate the band gap values of the synthesized oxides. This was achieved by generating Tauc plots, namely, a plot of the Kubelka-Munk function versus photon energy–($\alpha h\nu^n$ vs. hv).[122] Table 4-9 displays the experimental, calculated and reported band gap energy values. The resulting niobate products were observed to be white and dark brown for $ZnNb_2O_6$ and $CuNb_2O_6$ respectively (see Figure 4-29).

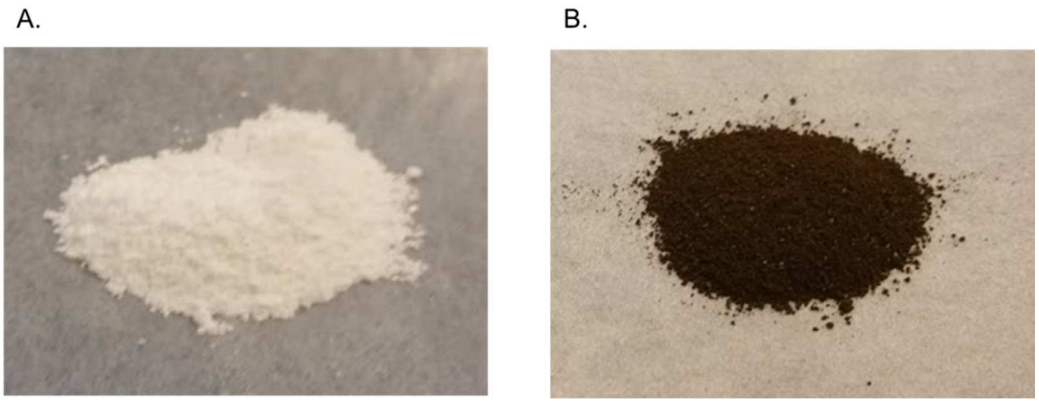

Figure 4-29 Photographs of A. $ZnNb_2O_6$ and B. $CuNb_2O_6$.

Table 4-9 Optical properties of the solution combustion synthesized niobate samples.

Sample	Band gap energy (eV)			
	As-synthesized	Annealed at 600°C	Calculated values	Reported values
$ZnNb_2O_6$	3.25 ± 0.02	3.55 ± 0.05	3.53	3.31 – 4.06 [115,155,156]
$CuNb_2O_6$	Not determined	1.77 ± 0.01	2.07	1.45 – 2.5[108,111,157]

An indirect band gap of 3.55 eV was obtained for $ZnNb_2O_6$. An additional band gap value of 3.22 eV was also determined corresponding to ZnO. See Figure 4-30 for the $ZnNb_2O_6$ Tauc plot. The $ZnNb_2O_6$ value lies within the range of previously reported

values as shown in Table 4-9. Figure 4-31 shows an indirect band gap value of 1.77 eV for the $CuNb_2O_6$ sample annealed at 600˚C.

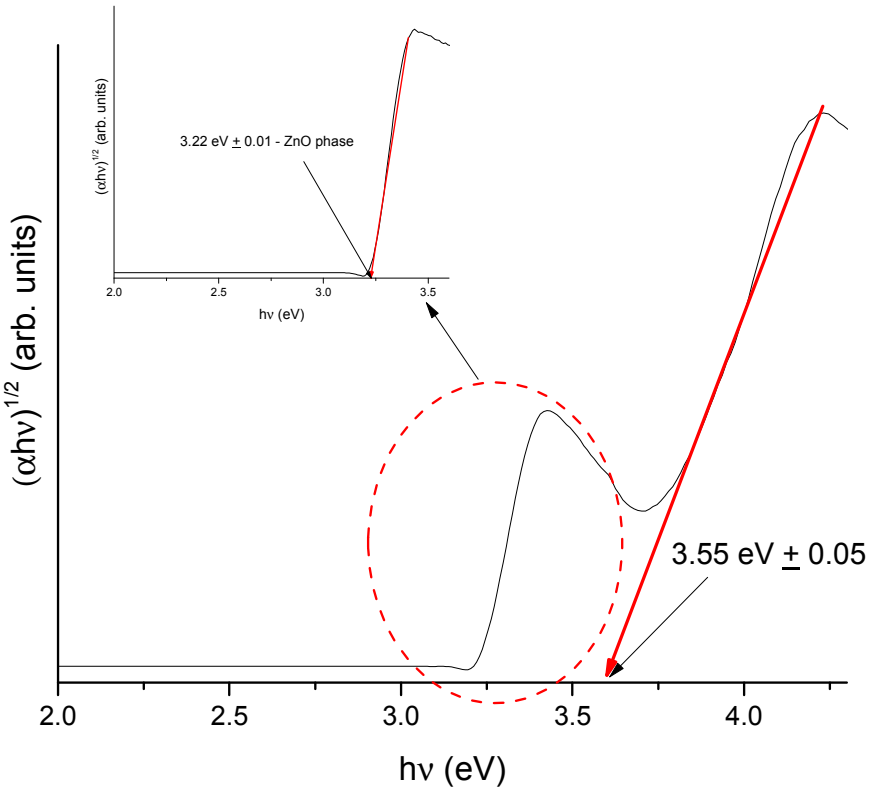

Figure 4-30 Tauc plot of $ZnNb_2O_6$ annealed at 600˚C. The insert shows the band gap determination for ZnO.

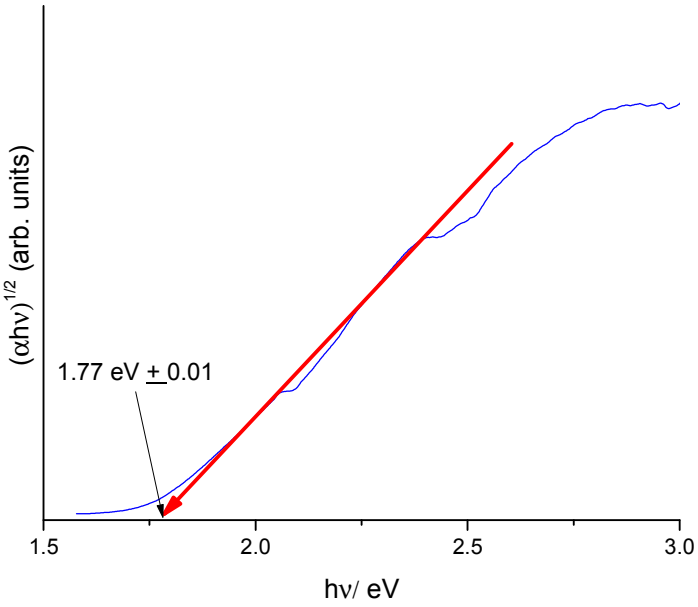

Figure 4-31 Tauc plot of $CuNb_2O_6$ annealed at 600˚C.

4.2.4. Electronic Band Structure Calculations

The electronic band structures for the SCS niobates were calculated along the special symmetry points in the Brillouin zone. The DFT + U electronic band structures of $ZnNb_2O_6$ and $CuNb_2O_6$ are shown above in Figures 4-29 A and B respectively. Figure 4-32 A exhibits an indirect band gap of 3.53 eV for $ZnNb_2O_6$ (very close to the experimental value) occurring along the Γ → X. The CB and the VB are mostly dispersive indicating lower effective masses for holes and higher effective masses for electrons respectively.

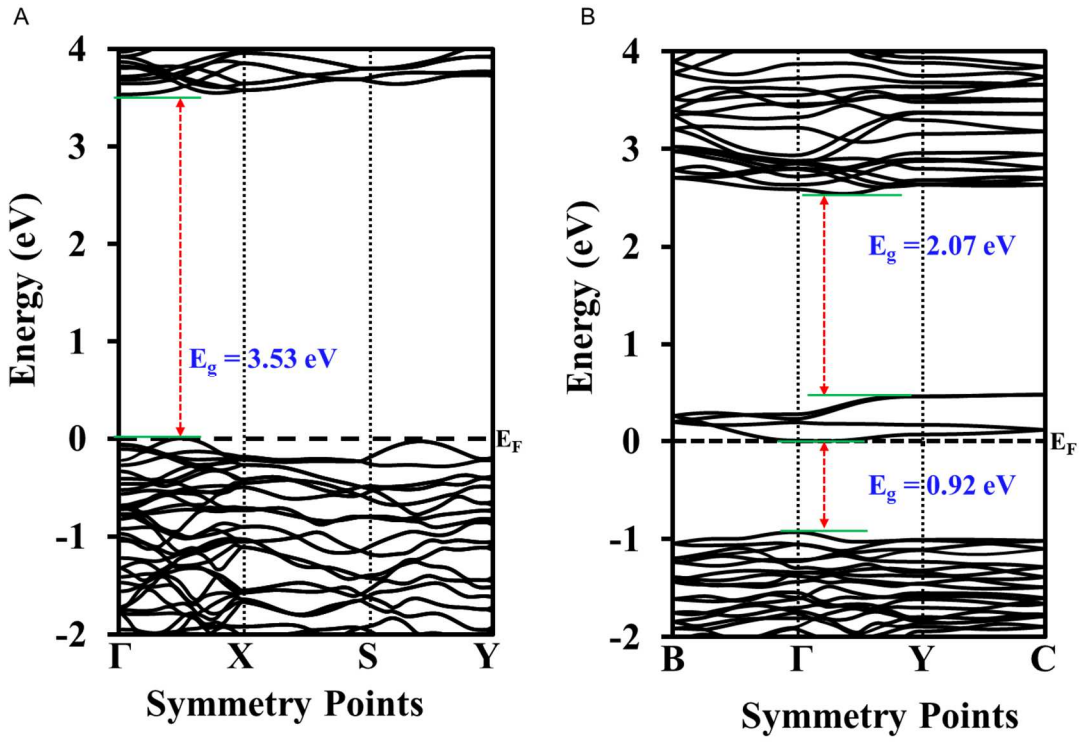

Figure 4-32 Electronic band structure of A. $ZnNb_2O_6$ and B. $CuNb_2O_6$.

(Courtesy Dr. Muhammed Huda's group – Physics Department)

While $ZnNb_2O_6$ has a net magnetic moment of 0 μ_B, $CuNb_2O_6$ has a net magnetic moment of 4.00 μ_B, thereby having different spin-up and spin-down contributions. The major difference in $CuNb_2O_6$ band structures in the two spin directions is the presence of partially occupied and unoccupied intermediate bands in the spin-down channel near the Fermi level as shown in Figure 4-32 B. The presence of intermediate bands splits the band gap of $CuNb_2O_6$ into two sub-band gaps: a direct band gap at Γ with a value of 0.92 eV, and the other one being indirect with a value 2.07 eV along Γ → C region. Very often

these partially occupied bands near Fermi level can contribute to the p-type conductivity of $CuNb_2O_6$. In $CuNb_2O_6$, although the presence of holes (p-type conductivity) is highly possible, the VB is relatively flat. As a result, despite their intrinsic presence, holes may not be very mobile, and hence conductivity due to holes may not be significant.

4.2.5. Photoelectrochemical Measurements

Photoelectrochemical results showed the characteristics of an n-type and a p-type semiconductor material for $ZnNb_2O_6$ and $CuNb_2O_6$ respectively (see Figures 4-33 and 4-34). A good photoresponse was displayed by the $ZnNb_2O_6$ material with two separate processes occurring: the oxidation of the sulfite ion up to -0.2 V and the oxidation of water above -0.2 V (Figure 4-33).

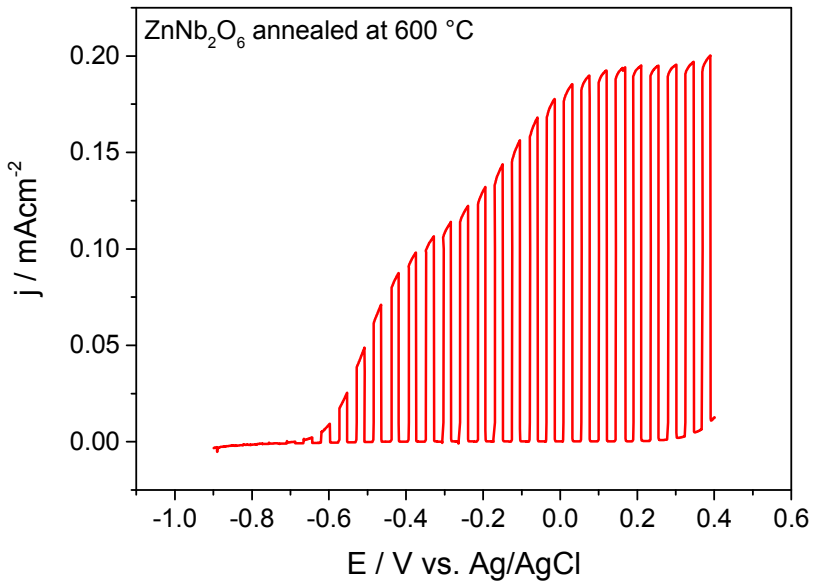

Figure 4-33 Photovoltammogram of $ZnNb_2O_6$ in 0.1 M Na_2SO_3 at a sweep rate of 2 mV/s using a 100 W Oriel UV lamp.

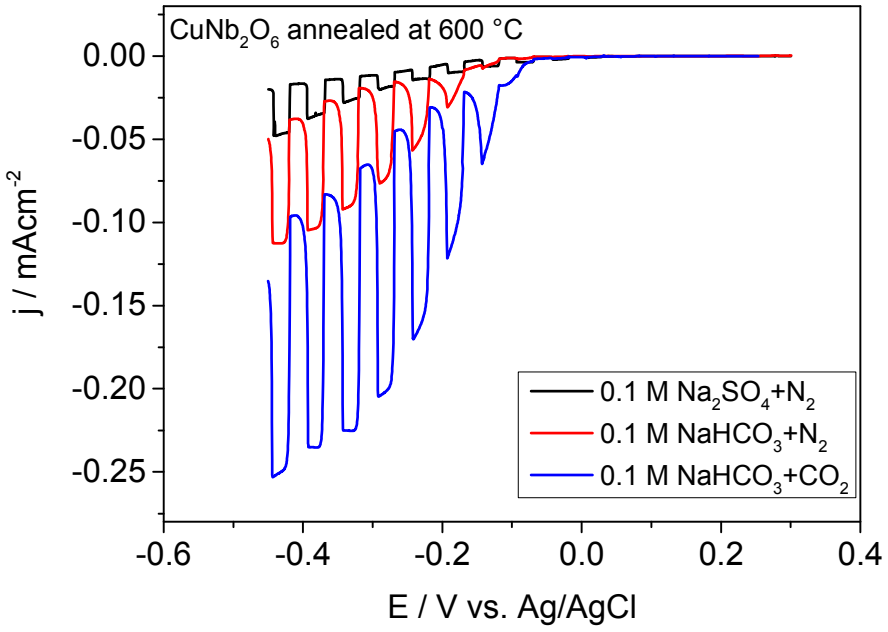

Figure 4-34 Photovoltammogram of $CuNb_2O_6$ at sweep rate of 1 mV/s using a Fiberlite visible lamp.

The $CuNb_2O_6$ material was analyzed under three varying conditions. A very low photoresponse was observed when using 0.1 M Na_2SO_4 + N_2. When the medium was changed to 0.1 M $NaHCO_3$ + N_2 a larger photoresponse was displayed suggesting that the process occurring is not limited to proton reduction. A significantly larger photoresponse curve was observed upon changing the gas from N_2 to CO_2, directly proving that the process occurring in this case is CO_2 photoreduction.

Chapter 5

Conclusions

In this overall study, binary tungstate and niobate nanoparticles $ZnWO_4$, $CuWO_4$, Ag_2WO_4 and $CuNb_2O_6$, $ZnNb_2O_6$ were successfully synthesized by solution combustion synthesis. In the case of the tungstates, two different tungsten precursors were used yielding a pure, monophasic structure for the samples synthesized with Na_2WO_4, and a biphasic structure with the $(NH_4)_2WO_4$ precursor. Most of the as-synthesized tungstates were crystalline in nature with an increased degree of crystallinity occurring with increasing annealing temperature. Raman spectroscopy and TEM images further confirmed the crystalline structures of each material, highlighting that the precursor materials play an important role in each material's morphology. The experimental optical properties correlated with literature survey as well as with computational data.

Good photocatalytic performance (relatively high k_{app}) was observed for the as-synthesized tungstates for the photodegradation of methyl orange dye with $ZnWO_4$ (Na) exhibiting the best photocatalytic activity. In-depth analysis of these reactions suggested that factors other than surface area contributed to a fast degradation process. Utilizing computational details as well as photoelectrochemical measurements, surface chemistry along with VB edge positions were shown to be key contributors in the high photocatalytic activity of $ZnWO_4$ compared to the other materials.

Copper niobate formed a single phase monoclinic structure, while a multiphase orthorhombic structure was observed for $ZnNb_2O_6$. Photoelectrochemical measurements showed an n-type and p-type semiconductor characteristic for the $ZnNb_2O_6$ and $CuNb_2O_6$ materials respectively. Additionally, CO_2 reduction occurred on the $CuNb_2O_6$ electrode surface upon visible light irradiation.

All in all, this study demonstrates that the use of SCS to synthesize these materials is very simple and quite versatile. It also illustrates that the insertion of desired metal ions into various structural frameworks e.g., WO_3, Nb_2O_5 can alter their optical and optoelectronic attributes for varied applications.

References

1. Rajeshwar, K. *J. Appl. Electrochem*. **2007**, *37*, 765 – 787.
2. Navarro Yerga, R. M.; Alvarez Galván, M. C.; del Valle, F.; a Villoria de la Mano, J.; Fierro, J. L. G. *ChemSusChem.* **2009**, *2*, 471 – 485.
3. Tao, M. Electrochem. Soc. Interface, **2008**, *17*, 30 – 35.
4. Rajeshwar, K. *J. Phys. Chem. Lett*. **2011**, *2*, 1301 – 1309.
5. Rajeshwar, K. Thomas, A.; Janaky C. *J. Phys. Chem. Lett.* **2015**, *6*, 139 – 147.
6. Linsebigier, A.; Lu, G.; Yates, J. *Chem. Rev.* **1995**, *95*, 735 – 758.
7. Fujishima, A.; Honda, K. *Nature* **1972**, *238*, 37 – 38.
8. Dingwang, C.; Ajay K. R. *Chem. Eng. Sci.* **2001**, *56*, 1651 – 1570.
9. Chenthamarakshan, C. R.; Rajeshwar, K.; Wolfrum, E. J. *Langmuir* **2000**, *16*, 2715 – 2721.
10. Rajeshwar, K.; de Tacconi, N. R. *Chem. Soc. Rev.* **2009**, *38*, 1984 – 1998.
11. Caballero, L.; Whitehead, K. A.; Allen, N. S.; Verran, J. *J. Photochem. Photobiol. A* **2009**, *202*, 92 – 98.
12. Sunada, K.; Watanabe, T.; Hashimoto, K. *J. Photochem. Photobiol. A* **2003**, *156*, 227 – 233.
13. Morales, W.; Carson, M.; Aina, O.; de Tacconi,N. R.; Rajeshwar, K. *J. Am. Chem. Soc.* **2008**, *130*, 6318 – 6319.
14. Janaky, C.; Rajeshwar, K.; de Tacconi, N. R.; Chanmanee, W.; Huda, M. N. *Catal. Today* **2013**, *199*, 53 – 64.
15. Hariharan, C. *Appl. Catal. A* **2006**, *304*, 35 – 61.
16. Wang, M.; Fei, G. T-; Zhang, L. D. *Nanoscale Res. Lett.* **2010**, *5*, 1800 – 1803.
17. Liu, Y.; Li, Y.; Zeng, H. *J. Nanomater.* **2013**, *69*, 1 – 9.
18. Domenech, J.; Prieto, A. *J. Phys. Chem*. **1986**, *90*, 1123 – 1126.

19. Leland, J. K.; Bard, A. J. *J. Phys. Chem*. **1987**, *91*, 5076 – 5083.
20. Kawahara, T.; Yamada, K.; Tada, H. *J. Colloid Interface Sci.* **2006**, *294*, 504 – 507.
21. Alagari, M.; Hamid, S. B. A. *Mater. Lett*. **2014**, *136*, 329 – 332.
22. Gondal, M. A.; Hameed, A.; Tamani, Z. H.; Suwaiyan, A. *Chem. Phys. Lett*. **2004**, *385*, 111 – 115.
23. Bessekhouad, Y.; D. Robert, D.; Weber, J.-V. *Catal. Today* **2005**, *101*, 315 – 321.
24. Zhang, L.; Wang, W.; Yang, J.; Chen, Z.; Zhang, W.; Zhou, L.; Liu, S. *Appl. Catal. A: Gen.* **2006**, *308*, 105 – 110.
25. Lin,G.; Tan, D.; Luo, F.; Chen, D.; Zhao, Q.; Qiu, J.; Xu, Z. *J. Alloys Compd.* **2010**, *7*, L43 – L46.
26. Zhou, B.; Liu, Z.; Wang, H.; Yang, Y.; Su, W. *Catal. Lett*. **2009**, *132*, 75 – 80.
27. McShane, C. M.; Choi, K. S. *J. Am. Chem. Soc.* **2009**, *131*, 2561 – 2569.
28. Rajeshwar, K.; de Tacconi, N. R.; Ghadimkhani, G.; Chanmanee, W.; Janáky, C. *ChemPhysChem.* **2013**, *14*, 2251 – 2259.
29. Kőrösi, L.; Papp, S.; Meyen, V.; Cool, P.; Vansant, E.; Dékány, I. *Colloids Surface A* **2005**, *268*, 147 – 154.
30. Yang, Z.; Lv, L.; Dai, Y.; Xv, Z.; Qian, D. *Appl. Surf. Sci*. **2010**, *256*, 2898 – 2902.
31. Wang, H.; Sun, F.; Zhang, Y.; Li, L.; Chen, H.; Wu, Q.; Yu, J. *J. Mater. Chem.* **2010**, *20*. 5641 – 5645.
32. Bard, A. J.; Faulkner, L. R. *Electrochemical Methods: Fundamentals and Applications*; 2nd Ed.; John Wiley & Sons: NJ, 2001.
33. Litter, M. I. *Appl. Catal.: Environ.* **1999**, *23*, 89 – 114.

34. Bhatkhande, D. S.; Pangarkar, V. G.; Beenackers, A. *J. Chem. Technol. Biotechnol.* **2001**, *77*, 102 – 116.
35. Wang, C.; Zhang, H.; Li, F.; Zhu, L. *Environ. Sci. Technol.* **2010**, *44*, 6843 – 6848.
36. Casals-Casas, C.; Desvergne, B.; *Annu. Rev. Physio.* **2011**, *73*, 135 – 162.
37. Hoffmann, M. R.; Martin, S. T.; Choi, W.; Bahnemann, D. W. *Chem. Rev*. **1995**, *95*, 69 – 96.
38. Vinu, R.; Madras, G. *J. Indian Inst. Sci*. **2010**, *90*, 189 – 230.
39. Rauf, M. A.; Ashraf. S. S. *Chem. Eng. J.* **2009**, *151*, 10 – 18.
40. Mishra, M.; Chun, D.-M. *Appl. Catal. A: Gen.* **2015**, *498*, 126 – 141.
41. Gaya, U. I.; Abdullah, A. H. *J. Photochem. Photobiol. C* **2008**, *9*, 1 – 12.
42. Hwang, C. –C.; Wu, T. –Y.; Wan, J.; Tsai, J. –S. *Mater. Sci. Eng. B* **2004**, *111*, 49 – 56.
43. Patil, K. C.; Hedge, M. S.; Rattan, T.; Aruna, S. T. *Chemistry of Nanocrystalline Oxide Materials: Combustion Synthesis, Properties and Application*; World Scientific Publishing Co. Pte. Ltd.: 5 Toh Tuck Link, Singapore, 2008; pp 345.
44. Lalena, J. N.; Cleary, D. A.; Carpenter, E. E.; Dean, N. F. *Inorganic Materials Synthesis and Fabrication*; John Wiley & Sons, Inc.: Hoboken, New Jersey, 2008,; pp 303.
45. Suchanek, W. L.; Riman, R. E. *Adv. Sci. Technol*. **2006**, *45*, 184 – 193.
46. Cundy, C. S.; Cox, P. A. *Micropor. Mesopor. Mat.* **2005**, *85*, 1 – 78.
47. Kaya, C.; He, J. Y.; Gu, X.; Butler, E. G. *Micropor. Mesopor. Mat*. **2002**, *54*, 37 – 49.
48. Segal, D. J. *Mater. Chem*. **1997**, *7*, 1297 – 1305.
49. Aruna, S. T.; Patil, K. C. *J. Mater. Synth. Proces.* **1996**, *4*, 175 – 179.

50. Smart, L. E.; Moore, E. A. *Solid State Chemistry: An Introduction*; 3rd Edition. CRC Press, Taylor & Francis Group, Boca Raton, Florida, 2005; pp 463.
51. Arutani, O.; Ogi, T.; Nandiyanto, A. B. D.; Iskandar, F.; Okuyama, K. *Inorg. Mater. Synth. Proces.* **2014**, *60*, 41 – 49.
52. Ivanova, I.; Gesheva, T. K.; Popkivov, G.; Ganchev, H.; Tzvetkova, E. *Mater. Sci. Eng. B* **2005**, *119*, 232 – 239.
53. Zhitomirsky, I.; Gal-or, L.; Kohn, A.; Henniche, H. W.; *J. Mater. Sci*. **1995**, *30*, 5307 – 5312.
54. Chen, Z.; Tang, Y.; Zhang, L.; Luo, L. *Electrochimica Acta* **2006**, *51*, 5870 – 5875.
55. Merzhanov, A. G. *J. Mater. Sci*. **2004**, *1*, 1779 – 1786.
56. Patil, K. C. *Bull. Mater. Sci*. **1993**, *16*, 533 – 541.
57. Patil, K. C.; Aruna, S. T.; Ekambaran, S. *Curr. Opin. Solid State Mater. Sci*. **1997**, *2*, 158 – 165.
58. Mukasyan, A. S.; Epstein, P.; Dinka, P. P. *Combust. Inst*. **2007**, *21*, 1789 – 1795.
59. Patil, K. C.; Aruna, S. T.; Mimani, T. *Curr. Opin, Solid State Mater. Sci.* **2002**, *6*, 507 – 512.
60. de Tacconi, N. R.; Timmaji, H. K.; Chanmanee, W.; Huda, M. N.; Sarker, P.; Janáky, C.; Rajeshwar, K. *ChemPhysChem.* **2012**, *13*, 2945 – 2955.
61. Watanabe, N.; Horikoshi, S.; Kawabe, H.; Sugie, Y.; Zhao, J.; Hidaka, H. *Chemosphere* 2003, *52*, 851 – 859.
62. Nagaveni, K.; Hegde, M. S.; Ravishankar, N.; Subbanna, G. N.; Madras, G. *Langmuir* **2004**, *20*, 2900 – 2907.
63. Sivalingam, G.; Nagaveni, K.; Hegde,M. S.; Madras, G. *Appl. Catal. B Environ.* **2003**, *45*, 23 – 38.

64. Kikkawa, S.: Hosokawa, S.: Ogawa, H. *J. Am. Ceram. Soc.* **2005**, *88*, 308 – 311.
65. Deshpande, K.; Mukasyan, A.; Varma, A. *Chem. Mater.* **2004**, *16*, 4896 – 4904.
66. Valdés, Á; Kroes, G. *J. Chem. Phys.* **2009**, *130*, 114701 – 114709.
67. Zhang, H.; Chen, G.; Bahnemann, D. W. *J. Mater. Sci.* **2009**, *19*, 5089 – 5121.
68. Kim, D. W.; Cho, I. –S.; Shin, S. S.; Lee, S.; Noh, T. H.; Kim, D. H.; Jung. H. S.; Hong, K. S. *J. Solid State Chem.* **2011**, *184*, 2103 – 2107.
69. Tian, J.; Sang, Y.; Yu, G.; Jiang, H.; Mu, X.; Liu, H. *Adv. Mater*. **2013**, *25*, 5075 – 5080.
70. Sun, S.; Wang, W.; Zhang, L.; Gao, E.; Jiang, D.; Sun, Y.; Xie, Y. *ChemSusChem.* **2013**, *6*, 1873 – 1877.
71. Zhang, L.; Bahnemann, D. *ChemSusChem.* **2013**, *6*, 283–290.
72. Cho, I.-S.; Kwak, C. H.; Kim, D. W. ; Lee, S. ; Hong, K. S. *J. Phys. Chem. C* **2009**, *113*, 10647 – 10653.
73. Ungelenk, J.; Feldmann, C. *Chem. Commun.* **2012**, *48*, 7838 – 7840.
74. Tang, J.; Zou, Z.; Ye, J. *J. Phys. Chem. B* **2003**, *107*, 14265 – 14269.
75. Song, S.; Zhang, Y.; Xing, Y.; Wang, C.; Feng, J.; Shi, W.; Zheng, G.; Zhang, H. *Adv. Funct. Mater.* **2008**, *18*, 2328 – 2334.
76. Kihlborg, L.; Gebert, E. *Acta Crystallogr. Sect. B Struct. Crystallogr. Cryst. Chem.* **1970**, *26*, 1020 – 1026.
77. Forsyth, J.; Wilkinson, C.; Zvyagin, A. *J. Phys. Condens. Matter* **1991**, *3*, 8433 – 8440.
78. Yourey, J. E.; Bartlett, B. M. J. Mater. Chem. 2011, 21, 7651 – 7660.
79. Thomas, A.; Janaky, C.; Samu, G. F.; Huda, M. N.; Sarker, P.; Liu, P. J.; van Nguyen, V.; Wang, E. H.; Schug, K. A.; Rajeshwar, K. ChemSusChem. **2015**, *8*, 1652 – 1663.

80. Van den Berg, A.; Juffermans, A. *J. Appl. Crystallogr.* **1982**, *820*, 10114 – 10116.
81. Cavalcante, L.; Almeida, M.; Avansi, W.; Tranquilin, R.; Longo, E.; Batista, N.; Mastelaro, V.; Li, S. *Inorg. Chem.* **2012**, *51*, 10675 – 10687.
82. Khyzhun, O. Y.; Bekenev, V. L.; Solonin, Y. M. *J. Alloys Compd.* **2009**, *480*, 184 – 189.
83. Tang, J.; Ye, J. *J. Mater. Chem.* **2005**, *15*, 4246 – 4251.
84. Kuzmin, A.; Purans, J. *Radiat. Meas.* **2001**, *33*, 583 – 586.
85. Kumar, G. B.; Sivaiah, K; Buddhudu, S.*Ceram. Int.* **2010**, *36*, 199 – 202.
86. Huang, G.; Zhang, C.; Zhu, Y.*J. Alloys Compd.* **2007**, *432*, 269 – 276.
87. Siriwong, P.; Thongtem, T.; Phuruangrat, A.; Thongtem, S. *CrystEngComm.* **2011**, *13*, 1564 – 1569.
88. Longo, D.; Volanti, V.; Longo, L.; Garcia, I.; Nogueira, M. A. P.; Almeida, A.; Pinheiro, M.; Ferrer, L. S.; Cavalcante, J. Andres, *J. Phys. Chem. C* **2014**, *118*, 1229 – 1239.
89. Hojamberdiev, M.; Zhu, G.; Xu, Y. *Mater. Res. Bull.* **2010**, *45*, 1934 – 1940.
90. Zhang, R.; Cui, H.; Yang, X.; Liu, H.; Tang, H.; Li, Y. *Micro Nano Lett.* **2012**, *7*, 1285 – 1288.
91. Ruiz-Fuertes, J.; Errandonea, D.; Segura, A.; Manjon, F. J.; Zhu, Z.; Tu, C. Y. *High Pres. Res.* **2008**, *28*, 565 – 570.
92. Naik, S. J.; Salker, A.V. *Solid State Sci*. **2010**, *12*, 2056 – 2072.
93. Montini, T.; Gombac, V.; Hameed, A.; Felisari, L.; Adami, G.; Fornasiero, P. *Chem. Phys. Lett.* **2010**, *498*, 113 – 119.
94. Nadaraia, L.; Jalabadze, N.; Chedia, R.; Antadze, M.; Khundadze, L. *IEEE Trans. Nuc. Sci.* **2010**, *57*, 1370 – 1376.
95. Huang, G.; Zhu, Y. *Mater. Sci. Eng., B* **2007**, *139*, 201 – 208.

96. Kalinko, A.; Kuzmin, A. *J. Lumin.* **2009**, *129*, 1144 – 1147.

97. Manchevaa, M.; Iordanovaa, R.; Dimitriev, Y. *J. Alloys Compd.* **2011**, *509*, 15 – 20.

98. Pullar, R. C. *J. Am. Chem. Soc*. **2009**, *92*, 563 – 577.

99. Zhang, Y. C.; Yue, Z. X.; Qi, X.; Li, B.; Gui, Z. L.; Li, L. T. *Mater. Lett*. **2004**, *58*, 1392 – 1395.

100. Hosogi, Y.; Shimodaira, Y.; Kato, H.; Kobayashi, H.; Kudo, A. *Chem. Mater*. **2008**, *20*, 1299 – 1307.

101. Pullar, R. C.; Okeneme, K.; Alford, N. M. *J. Eur. Ceram. Soc.* **2003**, *23*, 2479 – 2483.

102. Norwig, J.; Weitzel, H.; Paulus, H.; Lautenschläger, G.; Rodriguez-Carvajal, J.; Fuess, H. *J. Solid State Chem*. **1995**, *115*, 476 – 483.

103. Wahlström, E.; Marinder, B. -O. *Inorg. Nucl. Chem. Lett.* **1977**, *13*, 559 – 564.

104. Langbein, H.; Wölki, G. *Themochim. Acta* **1995**, *264*, 67 – 73.

105. Kratzheller, B.; Gruehn, R. *J. Alloys Comp.* **1992**, *183*, 75 – 84.

106. Amonpattoratkit, P.; Ananta, S. *Mater. Chem. Phys*. **2013**, *139*, 478 – 482.

107. Prasatkhetragarn, A.; Ketsuwan, P.; Ananta, S.; Yimnirum, R. *Mater. Lett*. **2010**, *64*, 1113 – 1116.

108. Joshi, U. A.; Palasyuk, A. M.; Maggard, P. A. *J. Phys. Chem. C* **2011**, *113*, 13534 – 13539.

109. Joshi, U. A.; Maggard, P. A. *J. Phys. Chem. Lett*. **2012**, *3*, 1577 – 1581.

110. King, N.; Sahoo, P. P.; Fuoco, L.; Stuart, S.; Doughtery, D.; Liu, Y.; Maggard, P. A. *Chem. Mater*. **2014**, *26*, 2095 – 2104.

111. Kamimura, S.; Murakami, N.; Tsubota, T.; Ohno, T. *Appl. Catal. B – Environ*. **2015**, *174 – 175*, 471 – 476.

112. Sato, M.; Hama, Y. *J. Solid State Chem*. **1995**, *118*, 193 – 198.

113. Ngamjarurojana, A.; Khamman, O.; Yimnirun, R.; Ananta, S. *Mater. Lett*. **2006**, *60*, 2867 – 2872.

114. Zhang, Y. C.; Fu, B.; Liu, Q. *J. Alloy Compd.* **2009***, 477*, 716 – 719.

115. Hsiao, Y. -J.; Fang, T. -H.; Ji, L. -W. *Mater. Lett.* **2010**, *64*, 2563 – 2565.

116. Dai, J.; Zhang, C.; Shi, L.; Song, W.; Huang, X. *Ceram. Int.* **2012**, *38*, 1211 – 1214.

117. Deshpande, V. V.; Patil, M. M.; Navale, S. C.; Ravi, V. *Bull. Mater. Sci*. **2005**, *28*, 205 – 207.

118. Kaufmann, E. N. *Characterization of Materials:* Volume 1, John Wiley & Sons Inc. Hoboken, New Jersey, 2003; pp 663.

119. Dollimore, D. *Anal. Chem*. **1990**, *62*, 44R – 50R.

120. Flewitt, P. E. J.; Wild, R. K. *Physical Methods for Materials Characterization* 2nd Edition, CRC Press, London 2003.

121. Kaufmann, E. N. *Characterization of Materials:* Volume 2, John Wiley & Sons Inc. Hoboken, New Jersey, 2003; pp 1392.

122. Murphy, A. B. *Sol. Energy Mater. Sol. Cells* **2007**, *91*, 1326 – 1337.

123. Kresse, G.; Joubert, D. *Phys. Rev. B* **1999**, *59*, 11 – 19.

124. Blöchl, P. *Phys. Rev. B* **1994**, *50*, 17953 – 17979.

125. Kresse, G.; Furthmüller, J. *Phys. Rev. B. Condens. Matter* **1996**, *54*, 11169 – 11186.

126. Kresse, G.; Furthmüller, J. *Comput. Mater. Sci.* **1996**, *6*, 15 – 50.

127. Perdew, J.; Chevary, J.; Vosko, S. *Phys. Rev. B* **1992**, *46*, 6671 – 6687.

128. Perdew, J.; Burke, K.; Ernzerhof, M. *Phys. Rev. Lett.* **1996**, *77*, 3865 – 3868.

129. Zhou, F.; Marianetti, C.; Cococcioni, M.; Morgan, D.; Ceder, G. *Phys. Rev. B* **2004**, *69*, 201101-1 – 201101-4.

130. Ganduglia-Pirovano, M. V.; Hofmann, A.; Sauer,J. *Surf. Sci. Rep.* **2007**, *62*, 219 – 270.

131. Anisimov, V.; Zaanen, J.; Andersen, O. *Phys. Rev. B* **1991**, *44*, 943 – 954.

132. Anisimov,V.; Solovyev, I.; Korotin, M.; Czyzyk, M.; Sawatzky, G. *Phys. Rev. B* **1993**, *48*, 16929 – 16934.

133. Solovyev, I.; Dederichs, P.; Anisimov, V. *Phys. Rev. B* **1994**, *50*, 16861 – 16871.

134. Methfessel, M.; Paxton,A. T. *Phys. Rev. B* **1989**, *40*, 3616 – 3621.

135. Monkhorst, H.; Pack, J. *Phys. Rev. B* **1976**, *13*, 5188 – 5192.

136. Sarker, P.; Prasher, D.; Gaillard, N.; Huda, M. N. *J. Appl. Phys*. **2013**, *114*, 133508 – 1 – 133508-10.

137. Sarker, P.; Al-Jassim, M. M.; Huda, M. N. *J. Appl. Phys*. **2015**, *117*, 035702-1 – 035702-13.

138. Prasher, D.; Chong, M.; Chang, Y.; Sarker, P.; Huda, M. N.; Gaillard, N. *Sol. Hydrog. Nanotechnol. VIII, SPIE Proc.* **2013**, *8822*, 88220E-1 – 88220E-7.

139. Momma, K.; Izumi, F. *J. Appl. Crystallogr.* **2008**, *41*, 653 – 658.

140. Izumi, F.; Momma, K. *Solid State Phenom.* **2007**, *130*, 15 – 20.

141. Barnes, J. S.; Schug, K. A. *J. Agric. Food Chem.* **2014**, *62*, 4322 – 4331.

142. Shi, R.; Wang, Y.; Li, D.; Xu, J.; Zhu, Y. *Apppl. Catal. B Environ*. **2010**, *100*, 173 – 178.

143. Li, C. -L.; Fu, Z. -W. *Electrochim. Acta* **2008**, *53*, 4293 – 4301.

144. Zhang, C.; Zhang, H.; Zhang, K.; Li, X.; Leng, Q.; Hu, C. *ACS Appl. Mater. Interfaces* **2014**, *6*, 14423 – 14432.

145. Shim, H.; Cho, I.;Hong, K.; Lim, A. -H.; Kim, D. -W. *J. Phys. Chem. C* **2011**, *115*, 16228 – 16233.

146. Shim, H. -W.; Lim, A. -H.; Lee, G. -H.; Jung, H. -C.; Kim, D. -W. *Nanoscale Res. Lett.* **2012**, *7*, 9 – 16.

147. Liu, Y.; Wang, H.; Chen, G.; Zhou, Y. D.; Gu, B. Y.; Hu, B. Q.; *J. Appl. Phys.* **1988**, *64*, 4651 – 4653.

148. Ross-Medgaarden, E.; Wachs, I. *J. Phys. Chem. C* **2007**, *111*, 15089 – 15099.

149. Basiev, T. T.; Karasik, A. Y.; Sobol, A. A.; Chunaev, D. S.; Shukshin, V. E. *Quantum Electron.* **2011**, *41*, 370 – 372.

150. Janaky, C.; de Tacconi, N. R.; Chanmanee, W.; Rajeshwar, K. *J. Phys. Chem. C* **2012**, *116*, 4234 – 4242.

151. Selvan, R. K.; Gedanken, A. *Nanotechnology* **2009**, *20*, 105602 – 105609.

152. Baiocchi, C.; Brussino, M. C.; Pramauro, E.; Prevot, A. B.; Palmisano, L.; Marcí, G. *Int. J. Mass Spectrom.* **2002**, *214*, 247 – 256.

153. Dai, K.; Chen, H.; Peng, T.; Ke, D.; Yi, H. *Chemosphere* **2007**, *69*, 1361 – 1367.

154. Rajeshwar, K. in *Electron Transf. Chem.* (Ed.: V. Balzani), Wiley-VCH, Weinheim, 2001.

155. Wu, W.; Liang, Z.; Ding, Z.; Zheng, H.; Wu, L. *Solid State Sci*. **2011**, *13*, 2019.

156. Zhou, Y.; Qiu, Z.; Lü, M.; Ma, Q.; Zhang, A.; Zhou, G.; Zhang, H.; Yang, Z. *J. Phys. Chem. C* **2007**, *111*, 10190.

157. Joshi, U. A.; Palasyuk, A.; Arney, D.; Maggard, P. A. *J. Phys. Chem. Lett*. **2010**, *1*, 2719.

Biographical Information

Abegayl Lorenda Shara-Lynn Thomas received her Ph.D in Analytical Chemistry from The University of Texas at Arlington in August 2015. Her work focused on synthesizing metal-based oxide semiconductor nanoparticles and applying them for environmental remediation processes. In fall 2014, she was afforded the opportunity for 8 months to intern at Sid Richardson Carbon & Energy Co. where she utilized her research knowledge and skill set to accomplish various projects assigned by the company. Abegayl is a native of Grenada and migrated to the United States in 2005. She received a Bachelor of Science degree in Chemistry from Midwestern State University in May 2008.